Grain boundaries in graphene grown by chemical vapor deposition

2013 New J. Phys. 15 035024

(http://iopscience.iop.org/1367-2630/15/3/035024)

New Journal of Physics
The open access journal for physics

Grain boundaries in graphene grown by chemical vapor deposition

László P Biró[1,3,4] **and Philippe Lambin**[2]

[1] Institute of Technical Physics and Materials Science, Centre for Natural Sciences, H-1525 Budapest, PO Box 49, Hungary
[2] Department of Physics of Matter and Radiations, University of Namur (FUNDP), 61 Rue de Bruxelles, B-5000 Namur, Belgium
E-mail: biro.laszlo@ttk.mta.hu

New Journal of Physics **15** (2013) 035024 (38pp)
Received 3 November 2012
Published 21 March 2013
Online at http://www.njp.org/
doi:10.1088/1367-2630/15/3/035024

Abstract. The scientific literature on grain boundaries (GBs) in graphene was reviewed. The review focuses mainly on the experimental findings on graphene grown by chemical vapor deposition (CVD) under a very wide range of experimental conditions (temperature, pressure hydrogen/hydrocarbon ratio, gas flow velocity and substrates). Differences were found in the GBs depending on the origin of graphene: in micro-mechanically cleaved graphene (produced using graphite originating from high-temperature, high-pressure synthesis), rows of non-hexagonal rings separating two perfect graphene crystallites are found more frequently, while in graphene produced by CVD—despite the very wide range of growth conditions used in different laboratories—GBs with more pronounced disorder are more frequent. In connection with the observed disorder, the stability of two-dimensional amorphous carbon is discussed and the growth conditions that may impact on the structure of the GBs are reviewed. The most frequently used methods for the atomic scale characterization of the GB structures, their possibilities and limitations and the alterations of the GBs in CVD graphene during the investigation (e.g. under e-beam irradiation) are discussed. The effects of GB disorder on electric and thermal transport are reviewed and the relatively scarce data available on the chemical properties of the GBs are summarized. GBs are complex enough nanoobjects so that it may be unlikely that two

[3] www.nanotechnology.hu
[4] Author to whom any correspondence should be addressed.

experimentally produced GBs of several microns in length could be completely identical in all of their atomic scale details. Despite this, certain generalized conclusions may be formulated, which may be helpful for experimentalists in interpreting the results and in planning new experiments, leading to a more systematic picture of GBs in CVD graphene.

Contents

1. Introduction

Graphene, one atom thick layer graphite, recently became the focus of attention of solid state physics, materials science, nanoelectronics and nanophotonics [1–4]. To fully exploit the extraordinary promises of this first truly two-dimensional (2D) material, the production of large size and good quality graphene layers has to be mastered. One of the most promising routes is the growth of graphene by chemical vapor deposition (CVD) on various metal surfaces [5, 6]. CVD on Cu seems to be perhaps the closest to fulfilling the demands of practical applications [7]. The grown graphene films are polycrystalline, with numerous grain boundaries (GBs), and their transport properties are one to two orders of magnitude below those of graphene films produced by micro-mechanical cleavage from highly oriented pyrolytic

graphite (HOPG) [1]. Additionally the GBs, if occurring in nanopatterned graphene [8], may have dramatic effects on the performances of various graphene-based nanodevices [9].

As numerous technologically relevant materials are polycrystalline, GBs are a cornerstone of most of our technologies. If the true atomic details of such, usually three-dimensional (3D), interfaces are to be considered, a complex geometrical problem with eight degrees of freedom has to be solved [10]. This may be further complicated by the particular chemical composition at such interfaces and the intercalation of regions with positionally disordered atoms between two crystallites [11, 12]. Additionally, a crystal structure different from that of the bulk of the crystallites may be present in the intergranular region separating the two crystallites [13]. Fortunately, in the case of graphene, the geometric complexity is reduced by reducing the dimensionality of the system to only 2, but further complications may arise due to the differences in the conditions under which the graphene GBs may be produced by using the different CVD methods developed recently [5], or the extreme temperature and pressure conditions used during high-temperature recrystallization of pyrocarbons. Indeed, a clear distinction should be made between exfoliated graphene either from HOPG or from natural graphite as both are produced at very high temperatures and high pressures (the conditions for HOPG production according to the procedure of Moore *et al* [14] are temperatures in the range of 3000 °C and pressures in the range of 4×10^7 Pa) and the graphene grown by CVD.

Even after recrystallization under the above extreme conditions, HOPG still contains GBs as evidenced by scanning tunneling microscopy (STM) [15]. These GBs may be observed usually in atomic resolution STM images, and will appear as a row of maxima in the tunneling current [16], due to the alteration of the local density of states, attributed to the presence of non-hexagonal rings in the honeycomb network [15, 17]. However, as one may expect, these GBs may be very different from those produced during CVD on Cu at around 1000 °C and at ambient pressure or below. The more so as, if certain CVD growth conditions are used, not the well-known Ostwald ripening [18] will occur but a Smoluchowski-type ripening may take place [19]. In the latter case, the diffusion and subsequent coalescence of large 2D islands constitute the dominant kinetic pathway to coarsening. Smoluchowski coarsening may be regarded as a consequence of the very strong C–C interaction and the weak C–Cu interaction [5].

The CVD growth itself is a very complex process and several methods have been developed [5] that established rather different values for the 'optimal' parameters depending on the use of different growth pressures, flow velocities, the kind of hydrocarbon used as carbon feedstock, hydrogen/hydrocarbon mixing ratios, growth tube geometries, etc. This many dimensional parameter space makes it very difficult to reach some simple and generally valid conclusions; nevertheless, it is worth exploring the experimental findings regarding the GBs along some selected lines of thought: (i) effects of the formation temperature of the GBs; (ii) effects of the pressure used in the CVD experiment; (iii) the differences due to solid or molten Cu substrate; (iv) advantages and drawbacks of the microscopic methods used in the study of the GBs; (v) effects of the GBs on transport; and last but not least the chemical properties of the GBs.

Most of the theoretical work on GBs is focused on that type of GBs which have been found in HOPG and which are built by incorporating non-hexagonal rings between two misoriented, but crystallographically prefect graphene lattices [20]. A recent modeling work considering more amorphous-like GBs has obtained interesting results [21], in good agreement with recent experimental data [22]. *Ab initio* simulations show that GBs may play a role in doping graphene, too [23]. A recent review summarizes from a mainly theoretical standpoint mostly the structure

and the properties of regular GBs [24], while placing less emphasis on the details of the GBs found experimentally in CVD graphene. Our paper is intended as complementary work in which the main emphasis is on the experimental side. A more general review of the structural defects in general in graphene was published recently [25].

As the structure and properties of the GBs may have dramatic effects on the transport properties [26], the mechanical behavior [21], the stability of the CVD graphene under ambient conditions [27] and the alteration of graphene properties by doping [23], understanding the formation, structure and properties of different kinds of GBs in CVD grown graphene will be critical for improving the quality of the material and for nanodevice manufacturing. Therefore, it seems useful to review the knowledge accumulated over the last few years on GBs in graphene grown by CVD. Although it is not within the scope of the present review, one should point out that GB engineering may also prove to be a useful tool in tuning the properties of a material [28]. At the present stage of the CVD growth of graphene, it seems premature to try to formulate some generally valid conclusions that could be equally correct for GBs formed during low-pressure and ambient pressure CVD (AP-CVD) or on solid or molten substrate. Nevertheless, the overview of the experimental findings may be helpful for the experimental work in interpreting the results and in planning new experiments, which could lead to a more systematic picture of GBs in CVD graphene.

A strong emphasis will be given to the STM, AFM and high-resolution transmission electron microscope (HRTEM) data as these experimental techniques are able to provide atomic scale information on the structure of the GBs, sometimes even on their formation. As Cu is the most widely used substrate used for the CVD growth of graphene, most examples will be given from CVD experiments on Cu. In some cases, other substrates will be mentioned, to illustrate particular aspects.

2. Structural models

GBs in graphene are often classified as ordered and disordered or as regular and amorphous. There is no clear consensus behind this classification, which will be useful only if one can attribute well-defined morphological or spectroscopic signatures to such GBs. In fact, precise criteria can be invoked when dealing with computer modeling. Accordingly, the following convention is used in this section: a disordered grain boundary is one that is obtained by merging two grains with irregular (disordered) edges. In contrast, connecting grains which both have a regular edge (e.g. along well-defined crystallographic directions) lead to ordered GBs.

A disordered GB has no reason to be a linear defect (see figure 1) and it should not show periodic modulations along it in the STM images (see figure 19(b)). Most likely, the carbon atoms in such a GB may not be perfectly threefold coordinated whereas in the regions where they are, there is a good chance that non-hexagonal rings exist. Information on how to model such disordered GBs on the computer can be found in [21]. In the approach used there, graphene grains with random orientation and random shape are grown by adding atoms on their borders until the space between the grains cannot accommodate further atoms. The whole structure is then annealed at high temperature by classical molecular dynamics based on the Tersoff–Brenner potential and finally quenched to an equilibrium state. As shown in figure 1(b), pentagons, heptagons and other non-hexagonal rings are abundant in the interfacial region between adjacent grains.

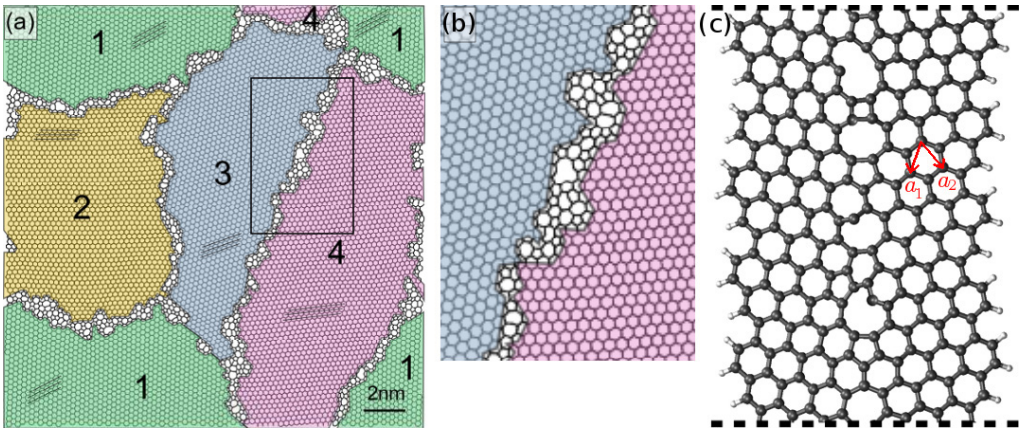

Figure 1. Examples of disordered GBs. (a) Polycrystalline graphene generated on the computer in a 20×20 nm box with periodic boundary conditions in the two directions (reproduced from [21], copyright (2012) by the American Physical Society). Zigzag directions in each grain are marked by sets of parallel lines. (b) Zoom of the area delimited by the rectangle drawn across the boundary between grains 3 and 4 in panel (a). (c) Boundary between two half-ribbons with thermally disordered $(9, 5)$ edges relative to the basis vectors shown by red arrows, the structure being saturated with hydrogen on its free edges and reproduced periodically along the vertical direction (adapted from [30]).

Another method allowing computer generation of polycrystalline graphene with periodic boundary conditions in the two directions is described in [29]. A rectangular super-cell with dimension $L_x L_y$, contains two graphene ribbons running parallel to the y-direction and having both a width close to $L_x/2$ in the transverse direction. The orientation of the crystallographic axes of one ribbon, which is mirror symmetric to that of the other ribbon, is chosen so as to fit with the L_y periodicity. In the x-direction, each ribbon is terminated at both ends in such a way so as to not overlap the other ribbon. The procedure makes it possible that the edges of the ribbons be irregular. Periodic boundary conditions are applied in that direction, too. The whole structure is relaxed at 0 temperature using the Brenner–Tersoff potential.

Using a somewhat similar method, although bringing structures closer to ordered GBs than disordered ones, Malola *et al* [30] cut two ribbons out of graphene with edges parallel to an arbitrary direction $\boldsymbol{R} = n\boldsymbol{a}_1 + m\boldsymbol{a}_2$, where $\boldsymbol{a}_1$ and $\boldsymbol{a}_2$ are the lattice vectors of graphene. One edge of both ribbons was passivated and molecular dynamics was applied to the atoms while increasing the temperature up to 1500 K. During this operation, the non-passivated edge of each ribbon conserves its direction R, but gets locally disordered. Next, one ribbon is rotated by 180° about its axis, translated by an arbitrary length along it, and is brought in close proximity to the other ribbon. The two pieces are then connected through tight-binding molecular dynamics and the obtained structure is finally optimized after cooling. Due to the 180°-rotational transformation of the first ribbon, the misorientation angle, here defined as the angle between the zigzag directions of the grains located on both sides of the GB[5], is twice

[5] Rather than resorting to Frank's formula as crystallographers often do, we use this geometrical definition, because the angle between zigzag (or armchair) directions is directly measurable in HRTEM pictures and in atomic-resolution STM or AFM images. In most instances, if not always, Frank's formula leads to a misorientation angle complementary of ours, namely $60^\circ - \tau$.

Table 1. Proportions of hexagons, pentagons, heptagons and octagons in the grain boundary region for three intervals of the misorientation angle τ. The rest is composed of squares and nonagons (compilation of data from [30]).

	Proportions (%)					
τ (deg)	Hexagons	Pentagons	Heptagons	Octagons	Rest	Remarks
0–15	63	18	12	5	2	Small-angle GB
15–45	36	24	22	12	6	Large-angle GB
45–60	55	11	8	13	13	Small-angle GB

the chiral angle of the vector $\boldsymbol{R}$,

$$\tau = (2/3)\ \sin^{-1}\{[nm(n+m)/2]/[(m^2+n^2+nm)/3]^{3/2}\}, \tag{1}$$

assuming that the angle between $\boldsymbol{a}_1$ and $\boldsymbol{a}_2$ is 60°. Figure 1(c) illustrates the result obtained for $n = 9$, $m = 5$ ($\tau = 41.2°$). Misorientations close to 0 and 60° lead to small-angle GBs, which are characterized by a small proportion of non-hexagonal rings, very often separated pentagon–heptagon pairs [31]. According to statistical data provided in [30], the numbers of polygons in the GBs vary in a complicated way with the misorientation angle. The average proportions of pentagons, hexagons, heptagons and octagons are listed in table 1 for three intervals of τ. For large angle GBs, it is clear from table 1 that non-hexagonal rings in the grain boundary region account for more than 60%. It is interesting to remark that the distribution of polygons versus τ is not symmetric with respect to $\tau = 30°$, as it should be.

An ordered GB is an ideal connection between two graphene half-planes having regular edges. Figures 5(c) and (d) in the next section illustrate how this construction can be initiated, the cumbersome part of it being the way in which the two grains are connected while keeping a threefold coordinated network. This requires adding or removing atoms from the interfacial region and optimizing the structure. The two connected halves must present a misorientation angle to form a grain boundary, although it is perfectly conceivable that both parts have the same orientation provided they are translated relatively to each other by a fractional lattice parameter. An example of such a *non-tilted* interconnected structure, actually observed experimentally in graphene grown on Ni(111) [32], can be obtained by a periodic alternation of pairs of edge-sharing pentagons and octagons in a direction parallel to the zigzag one (see figure 2(a)). The periodicity of this line defect is twice the lattice parameter of graphene, 0.49 nm, which is very short.

In the model of figure 4, the misorientation angle is 39°. This model is special in the sense that the GB direction is a mirror symmetry. It is made of a succession of pentagon–heptagon pairs aligned parallel to the GB line and separated by a hexagon edge, the periodicity being 0.65 nm. It is possible to construct another large-angle grain boundary in which the pentagon–heptagon pairs are connected to each other, without hexagons in between (see figure 2(b)), while meandering about the GB direction with a wavelength of 0.88 nm [33, 34]. The misorientation angle in that case is 28°. In these structures, according to the classical description of GBs in crystals [35, 36], the grain boundary is linear and consists of a chain of dislocations materialized by pentagon–heptagon pairs [33].

The GB having the largest misorientation ($\tau = 30°$) is one in which two graphene half-sheets with zigzag and armchair orientations, respectively, are joined together. This construction

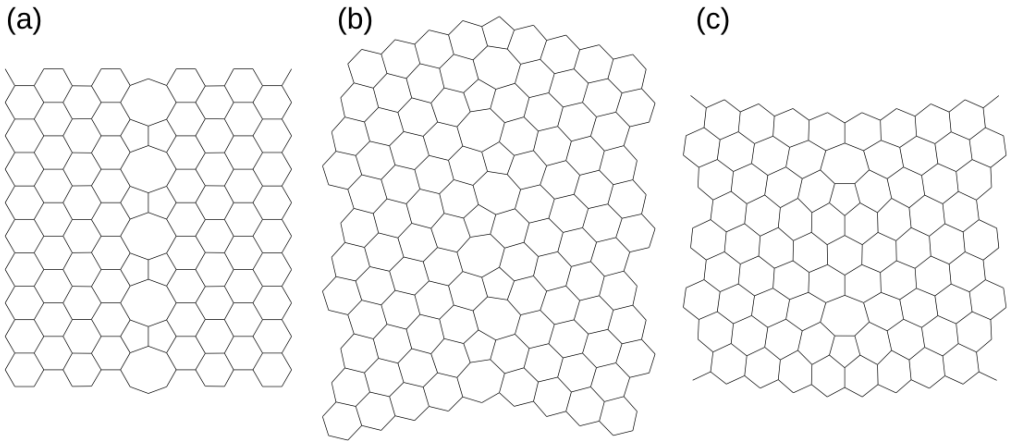

Figure 2. Examples of ordered GBs. All the models shown in this figure were relaxed with the Brenner–Tersoff potential. (a) Two translated graphene half sheets with parallel zigzag edges (no tilt angle) interconnected through alternating pentagon pairs and octagons [32]. (b) Grain boundary realized with adjacent pentagon–heptagon pairs, obtained by joining two grains with edges parallel to the direction $(1, 3)$ relative to the same set of lattice vectors $\boldsymbol{a}_1$ and $\boldsymbol{a}_2$ as in figure 3 (misorientation angle $\tau = 27.8^\circ$). (c) Grain boundary with index $(3, 2)$ in the notation of [20], with misorientation angle $\tau = 46.8^\circ$, shaped into a linear chain of pentagon–heptagon pairs separated by three transverse rows of hexagons.

is not simple to achieve, because the periodicities of the two lattices along the separation line are not commensurate. In [37], finite-width models of the $\tau = 30^\circ$ GB are proposed; the largest one is made of 25 and 14 unit cells of graphene ribbons with zigzag and armchair orientations, respectively. The model is fully optimized and contains seven pentagons and seven heptagons placed side by side.

The so-called coincidence lattice site method [20] can be used to generate models of ordered GB for all misorientation angles ranging between 0 and 60°. Geometrically, the idea behind this method is to superimpose exactly two graphene networks, and then to rotate one network relative to the other about a [001] axis issued from an arbitrary common site until a subset of lattice sites of both networks exactly fall back onto each other, thus forming a graphene bilayer with commensurate rotational fault [38]. The grain boundary is obtained by cutting the two honeycomb networks along a line going through coincident lattice sites. One half of a graphene located on one side of this line is conserved together with this half of the second graphene that is located on the other side of the cutting line (see figure 3). The two halves are connected together while rearranging the positions of the non-coincident lattice sites and optimizing the structure with classical potentials. This construction is easier when the two starting graphene networks are rotated clockwise and anticlockwise by the same angle. The cutting line can then be chosen along a mirror plane of the obtained moiré pattern, which is the case illustrated in figure 3. In these conditions, the GB orientation can be defined by two integer indices (n, m), namely the crystallographic coordinates of a site through which it goes relative to the Bravais vectors of one of the two rotated networks [20]. The misorientation angle then

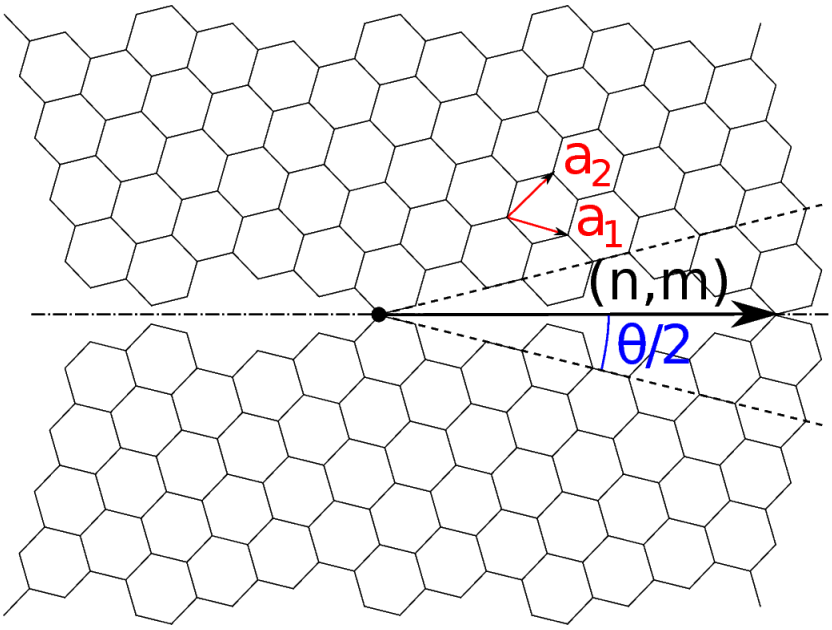

Figure 3. Two initially superimposed graphene sheets have been rotated about a common atom (black circle) in opposite directions and by the same angle $\theta/2$ such that a superlattice of atoms still coincides after the rotation (moiré coincidence). Half of each sheet has been removed on both sides of an initially common armchair direction (dot-dashed line) containing the rotation center. This armchair direction becomes a grain boundary that will be achieved by adding atoms and bonds in the holes between the two sheets. The GB is characterized by the translation vector of the moiré superlattice (thick arrow line) with indices (n, m) relative to the Bravais vectors $\boldsymbol{a}_1$ and $\boldsymbol{a}_2$ of the rotated upper sheet [20]. The drawing illustrates the particular case $n = 5$, $m = 2$ ($\theta = 27.8°$, $\tau = 32.2°$, equation (1)).

follows from equation (1). In these notations, figure 4 in the next section corresponds to the GB with indices (2, 1). The two grains have been rotated symmetrically in opposite directions by 10.5° each ($10.5° = (60° - 39°)/2$), the initially common armchair direction coinciding with the GB line. It is readily possible to generalize the symmetrical GB model of figure 4 by adding lines of hexagons between the pentagon–heptagon pairs [39]. In the notations of [20], the obtained GBs have the generic formula $(m + 1, m)$ when the number of lines of hexagons between two successive pentagon–heptagon pairs is $2m - 1$ ($m = 1, 2, \ldots$). The case $m = 2$ is illustrated in figure 2(c). Structural models of that sort are shown in [34], together with other structures where the separation distances between the pentagon–heptagon pairs are alternatively shorter and longer. In all these models, the GB misfit angle decreases as the density of pentagon–heptagon pairs decreases.

In all structural models constructed from graphene in free space, GBs do not yield an overall flat structure due to the presence of non-hexagonal rings. The GBs can lead to complicated 3D landscapes [31], and more so in the neighborhood of isolated pentagons or isolated heptagons, if any. In most instances, graphene samples lie on a support whose van der

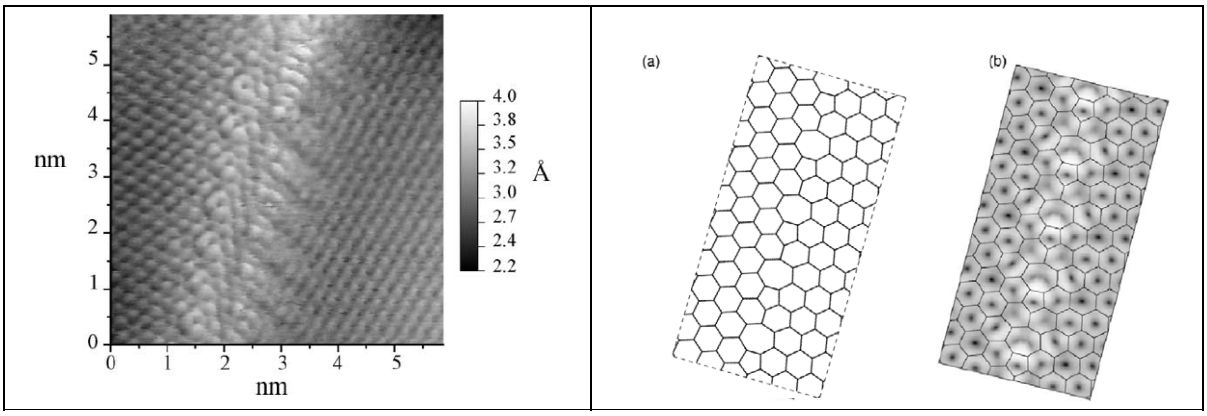

Figure 4. Experimental, constant current topographic STM images (left) showing the atomic scale appearance of grain boundary in the topmost layer of HOPG and the model structure (right): (a) the structural model; and (b) the computed STM image superimposed on the structural model (adapted from [15], copyright (2002), with permission from Elsevier).

Waals attraction constrains partly the vertical relaxation of the structure in the region of the GB, which reduces the structural topography. Nevertheless, the 3D features of a grain boundary are observable by STM (see section 6 for more detail).

3. Effects of the formation temperature on the structure of the grain boundaries

3.1. Grain boundaries in highly oriented pyrolytic graphite

As already mentioned above, HOPG is produced under extreme conditions, under which the survival of amorphous regions is unlikely. HOPG has a mosaic-like structure with crystalline grains of 10 μm size. Depending on the HOPG quality, the misorientation of the normals to the basal plane (c-axis) of neighboring crystallites may be below 1° or of the order of several degrees [40–42]. HOPG has been widely used for several decades as a test and calibration sample in STM; therefore the first observations of GBs in HOPG were reported quite early [43, 44]. Later on, more detailed studies followed in which a likely atomic structure for the observed periodic features in the atomic resolution STM images was proposed and the corresponding STM images were computed and compared with the experimental observations [15]. Good agreement was found between the computed and experimental data as shown in figure 4.

In more recent STM images acquired in UHV on cleaved HOPG samples, which after the loading in the UHV system were annealed at 500 °C, GBs appearing as linear and periodic superlattices were observed. It was found that the GBs changed in periodicity when changing the orientation of the superlattice by 30 or 90° with respect to the graphite lattice (figure 2 in [16]). Scanning tunneling spectroscopy (STS) and AFM measurements (in ambient air) were carried out, too. Topographic AFM images showed that the GBs appear as lines protruding above the graphite surface by a small height up to 0.3 nm. On the other hand, in topographic STM images, GBs show a periodic one-dimensional (1D) superlattice with height corrugations from 0.4 nm up

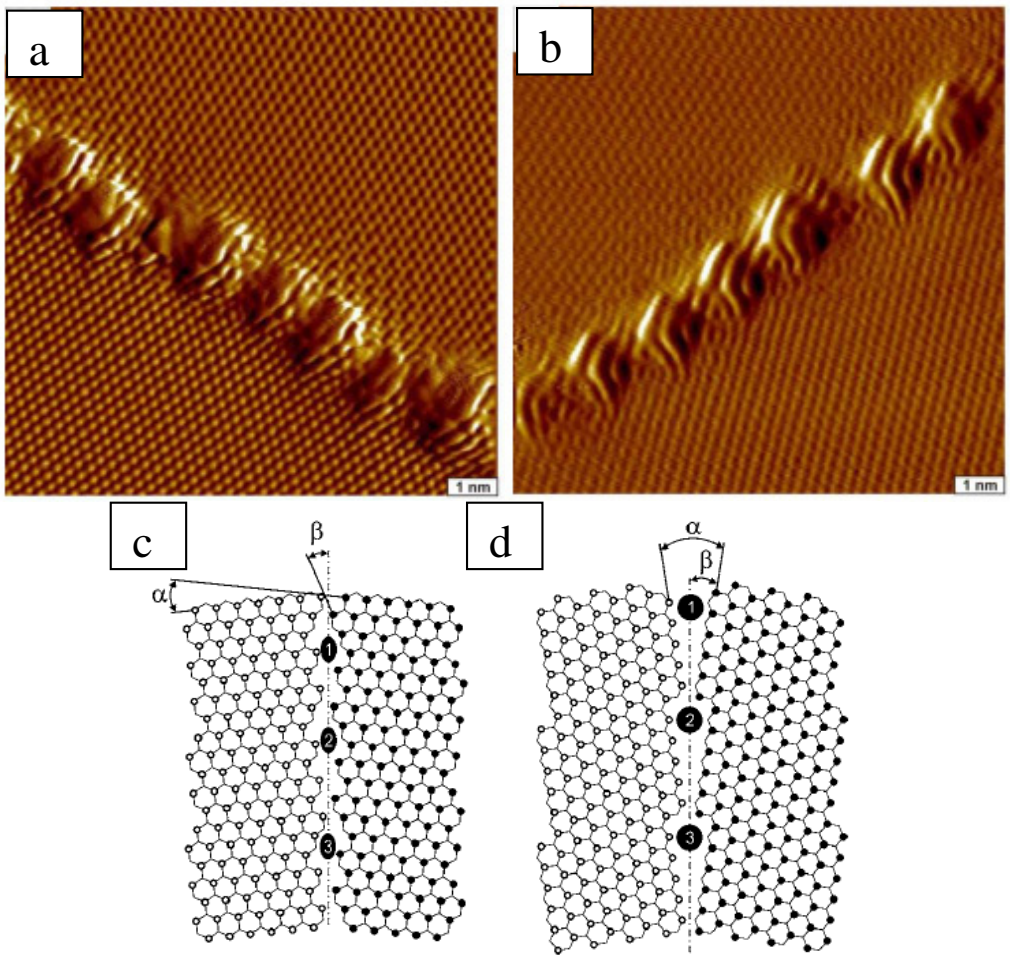

Figure 5. Atomic resolution STM images of two GBs exhibiting superlattices of different periodicities (a) and (b) and the proposed structural models (c) and (d). Scanning parameters: $10 \times 10\,\mathrm{nm}^2$, $U_\mathrm{b} = 0.5\,\mathrm{V}$ and $I_\mathrm{t} = 0.3\,\mathrm{nA}$. In (a), the periodicity is $D_1 = 1.25\,\mathrm{nm}$ and $\alpha = 12^\circ$, in (b), the periodicity is $D_2 = 1.4\,\mathrm{nm}$ and $\alpha = 18^\circ$. In (c), $\alpha = 12^\circ$, $D_1 = 1.18\,\mathrm{nm}$ and (d) $\alpha = 18^\circ$, $D_2 = 1.36\,\mathrm{nm}$. Note that in (a) and (c), armchair edges face each other, while in (b) and (d), zigzag edges (adapted from [16], copyright (2009) by The American Physical Society).

to 1.5 nm, which are almost independent of the applied bias voltage [16]. The above differences in height measured by AFM and STM indicate that the electronic properties of the GBs are different from the bulk of the graphite crystallites separated by the GBs. The different electronic structure in the GB region is responsible for the increased height measured by STM. GBs of different periodicities were found by atomic resolution STM, as figure 5 beautifully illustrates. One may note that the tunneling current maxima (light colors) have an arrangement typical of a certain GB.

The model structures in figures 5(c) and (d) are difficult to reconcile with the extreme conditions under which HOPG is produced. Under those conditions, a turbostratic structure with rough graphene layers is transformed into a close to perfect crystal. It seems unlikely that during such extensive structural modifications, such structures could survive unaltered.

It is more likely that structural rearrangements such as those discussed in section 2 will take place. The tunneling current maxima may be associated with the non-hexagonal carbon rings inserted in the honeycomb lattice. The very same reasoning should be valid for the graphene exfoliated from HOPG.

It was found by STS [16, 45] that the presence of the GBs induces localized states at −0.3 eV and at 0.4 eV. The alterations of the electronic structure may extend as far as 4 nm from the GB, with an exponential decay versus the distance from the GB [16]. The statistical distribution of the localized states shows that both the −0.3 eV and the 0.4 eV occur with a similar high frequency and are found for GBs exhibiting a superstructure periodicity smaller than 4 nm (about 80% probability of occurrence), while localized states around the Fermi level are much more rare in HOPG and are usually found for GBs exhibiting a superstructure periodicity larger than 4 nm [45].

An unusual STM image found on the two sides of a grain boundary on cleaved HOPG is reported in [46]. In the same STM image, a normal triangular lattice is seen on one side of the GB while on the other side, a honeycomb lattice shows up. This latter finding may indicate the decoupling of the topmost layer from that underneath on the side where the honeycomb lattice is observed. The experiment was performed in UHV. The sample was pretreated for 24 h in dichlorethane to facilitate the production of moiré patterns [46]. One cannot exclude that these treatments are responsible for the decoupling of graphene layers.

In summary, the GBs observed experimentally in HOPG, which by definition is a bulk material, so that HRTEM cannot be an option, indicate that the most frequent GBs are of the kind termed regular (see section 2). Therefore, the GBs which can be expected in the samples produced by cleavage from HOPG will also be of this particular kind.

3.2. Grain boundaries in epitaxial graphene on SiC

The epitaxial growth of graphene and few-layer graphite (FLG) on 4H-SiC may be regarded as being intermediate in temperature between the conditions of HOPG production and graphene CVD. Atomic resolution STM investigation revealed that even in the temperature range of 1500 °C, extended disorder may be present in the region of the GBs [47] in graphene grown on 4H-SiC(000$\bar{1}$). GBs of the type occurring in HOPG, appearing as linear defects composed of periodic tunneling current maxima [47], were found in the FLG grown on SiC, too. It is reported that the disordered GBs are occurring in the 'rough graphene' grown slightly below 1500 °C (figure 6), while the GBs composed of periodic tunneling current maxima are observed on the 'smooth graphene' grown slightly above this temperature. The rise in growth temperature is associated with a transition from rough graphene layers (seen regularly at 1475 °C) to uniform atomically smooth FLG having an atomic periodicity identical to HOPG (seen regularly at 1550 °C) [47].

Moiré type superlattices are also observed on the FLG grown on 4H-SiC, and their occurrence also shows temperature dependence. It is well known that such superstructures appear in the STM images when the topmost graphene layer and the one below are rotated with respect to each other; such structures can be produced on purpose by STM manipulation on the surface of HOPG [48, 49]. Under the growth conditions used in [47], moiré regions are never found as isolated structures surrounded by flat graphene layers, but they are associated with ridges observed in the STM images. Moiré regions are common on FLG samples grown at 1500 °C, rare on 1550 °C samples, and never found on 1600 °C samples. The ridges, next to

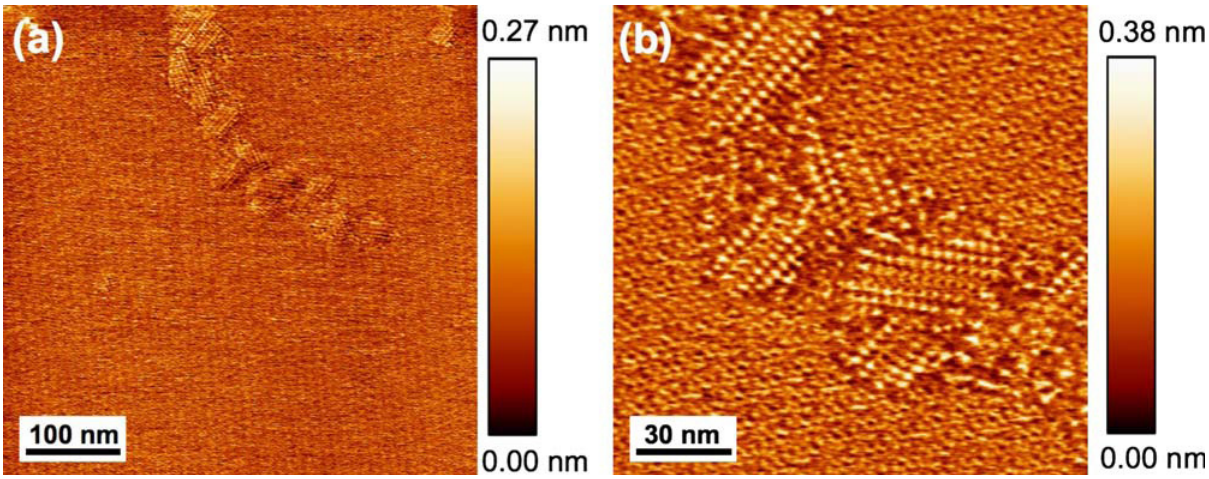

Figure 6. STM images of a region from the graphene grown on 4H-SiC at 1500 °C. In (a), a $500 \times 500\,\text{nm}^2$ image showing the presence of a grain boundary in the upper half of the image. In (b), a $150 \times 150\,\text{nm}^2$ image showing the parallel 1D features within the grain boundary. Scan parameters are $I_t = 2.0\,\text{nA}$ and $V_b = 100\,\text{mV}$ for (a) and (b) (reproduced from [47], copyright (2009) by The American Physical Society).

which the moiré regions are usually found, have high aspect ratios at 1500 °C but are smoother and more rounded at 1600 °C [47]. It is suggested that the observed moiré patterns form when two independently nucleated graphene regions growing toward each other merge, or when non-hexagonal rings incorporated into the growing graphene cause the rotation of the graphene lattice.

The above findings indicate that even in the temperature range of 1500 °C, structural defects are fairly stable in the graphene network, but this temperature seems to separate two different regimes in which the survival rate of defects is different.

At the somewhat lower growth temperatures (in the range of 1150 °C, determined with some uncertainty by a pyrometer) used to grow FLG (three to five layers) on the C face of the 6H-SiC, GBs of mixed character were reported in STM images [50]. In this respect, the GBs shown in figure 7 separate two regions, one of which clearly reveals a moiré type pattern, whereas in the other region, only the atomic resolution structure of graphite and the well-known superstructure due to electron scattering are seen. Elevated regions (appearing as white hills in the image)—some of which also exhibited a graphite-like atomic resolution [50]—are separated by flat regions in which atomic resolution was possible. The presence of the elevated regions can be regarded as a strong indication of non-hexagonal rings being inserted between the grains in the two topmost graphene layers, or in the layer below. While such structures are regularly observed on the C face of SiC, apparently they are absent on the Si face [50]. This may indicate the effect of the substrate interaction, which in the case of SiC is known to be strong more particularly on the Si face [51]. It is concluded in the paper that there is significant azimuthal disorder in the FLGs grown on the C face, which is both between the grains and inside the grains (stacking disorder).

The strongly meandering character of the GB seen in figure 7 makes it very unlikely that the GB separating the topmost graphene layers could be a regular GB. Additionally, the flat regions exhibiting atomic scale details, separating the protruding white regions in which no

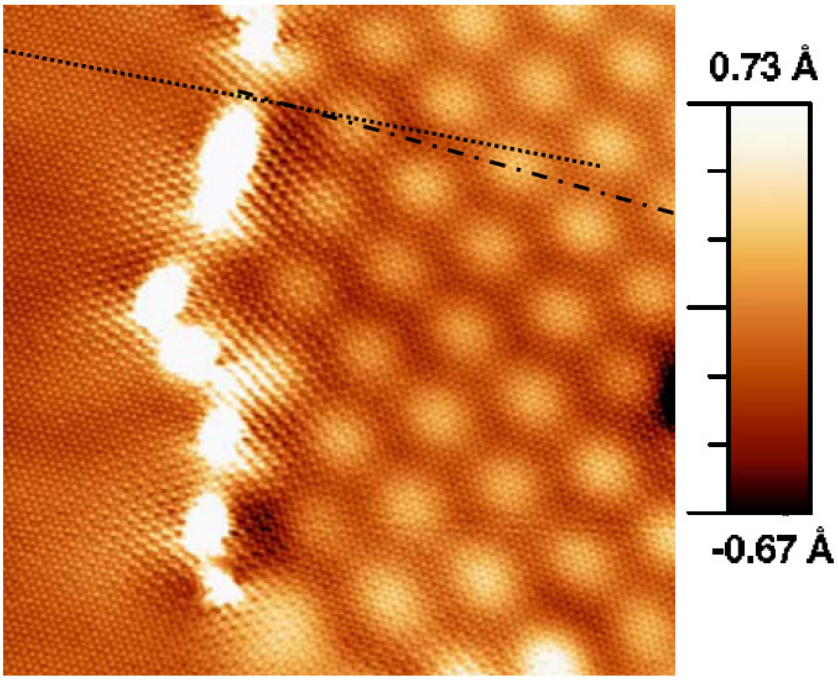

Figure 7. FLG grown on 6H-SiC, atomic resolution STM image in the region of the grain boundary revealed by moiré pattern. Image size is $20 \times 20\,\mathrm{nm}^2$, $V_b = -0.25\,\mathrm{V}$, and $I_t = 0.1\,\mathrm{nA}$. The dotted (dashed) line underlines the direction of the atomic rows in the left (right) part of the image, with a relative angle of 5° (reproduced from [50], copyright (2008) by The American Physical Society).

atomic details are seen, are arranged in a non-periodic way. This constitutes a further argument for a GB which does not fulfil the conditions of a regular GB. Taking into account that the GB was formed at 1150 °C, it is then not so surprising that there occurs extended disorder in the GBs formed at around 1000 °C during the CVD growth on solid Cu.

3.3. Grain boundaries in chemical vapor deposition grown graphene on Ir(111)

Despite the fact that Ir(111) exhibits several differences from the most frequently used polycrystalline Cu foils for the CVD growth of graphene, it can be very useful to gain insight into the formation of GBs on Ir due to the fact that a characteristic superstructure makes possible the observation of atomic size details on a larger scale than is usually needed for atomic resolution images.

An interesting comparison of graphene island morphologies is reported on Ir(111) [52]. Two growth methods were employed: room temperature adsorption and thermal decomposition at 597–1197 °C (temperature programmed growth (TPG)) as well as direct exposure of the hot substrate at 597–1047 °C (CVD); ethene was used as the carbon source. The temperature- and exposure-dependent growth of graphene was investigated in detail by STM. The growth experiments were carried out in UHV on a carefully cleaned Ir(111) surface. In TPG the room temperature adsorption of the molecules was followed by pyrolysis and graphene growth at a fixed elevated temperature; the growth was observed by STM, using a heating interval of 20 s

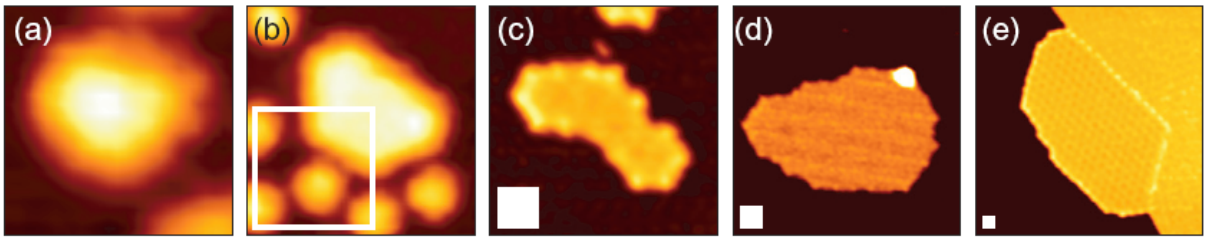

Figure 8. STM topographs of typical graphene islands prepared with the TPG procedure on Ir(111), after annealing for 20 s to (a) 598 °C, 3.2 nm × 3.2 nm, (b) 697 °C, 6.2 × 6.2 nm, (c) 847 °C, 18 nm × 18 nm, (d) 1047 °C, 32 nm × 32 nm and (e) 1197 °C, 64 nm × 64 nm. The size of the white box corresponds to the size of the smallest topographic image (3.2 nm × 3.2 nm). The islands undergo a transition from an undefined, probably amorphous state to a compact shape at low temperature to non-compact shapes at intermediate temperature and (c) back to more compact shapes at high temperature (reproduced from [52]).

at different temperatures (598, 697, 847, 1047 and 1197 °C). The typical shape and size of the islands are shown in figure 8.

It was found that the decomposition of ethene and the carbon cluster formation are completed in the range of 527 °C, the formation of graphene takes place at a temperature between 597 and 697 °C and, in the system studied, the edges are predominantly of zigzag type. Coarsening occurs via Smoluchowski ripening, i.e. graphene island diffusion and coalescence [52]. The different island morphologies are interpreted as follows: at 847 °C, small compact graphene islands with dense packed step edges touch during island diffusion and coalesce. However, as the time needed to reshape an island to its compact, minimum energy shape is a strongly increasing function of island size (it increases by the power 3–4 of the diameter of the final compact island), coalesced islands are not able to reshape on the timescale of the TPG experiment. After TPG at higher temperatures, the mobile graphene islands are found to be nearly completely pinned at steps. Once the graphene islands stick to steps, their mobility along the step is likely to be reduced as compared with the mobility on terraces; coalescence becomes thus rare and the islands have again sufficient time to reshape to a compact shape [52].

In CVD experiments, a hot Ir surface at 847 °C was employed. The following observations were made: (i) graphene is exclusively located at the substrate step edges for low coverages, (ii) graphene frequently spans both sides of the step edge, (iii) the larger fraction of graphene is on the lower terrace and (iv) while there are graphene flakes attached only to an ascending step edge, no graphene flakes were ever observed attached only to a descending step edge [52]. The coalescence of the graphene island can be monitored using the moiré pattern characteristic of graphene on Ir(111) [53]. In figure 9, the coalescence of two graphene islands is seen; the moiré pattern clearly shows their misorientation. Obviously, the hole in the center separating the two islands and the two narrow ‘fjords’ on the two sides have very small chances to be perfectly filled by a small island arriving in later growth steps. The characteristic island morphology for the temperature of 847 °C (figure 8(c)) is of an irregular shape; it seems unlikely that in this temperature range all the GBs formed during CVD growth may be constructed only by the incorporation of non-hexagonal rings. In a continuous CVD process, the ‘fjords’ seen in

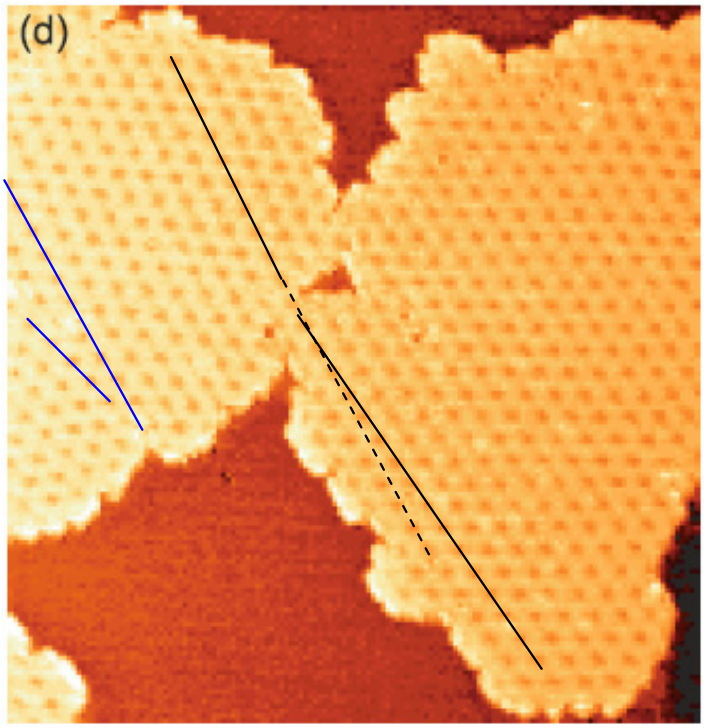

Figure 9. STM topograph (70 nm × 73 nm) of graphene grown by CVD on an Ir(111) surface at 847 °C, out of exposure to an ethene partial pressure of 5×10^{-10} mbar, for 20 s; two coalesced islands forming a coherent graphene island; the misorientation is evident from the deviation in the orientation of the rows of minima in the STM images (highlighted with black lines). Note that the left-hand side island, in fact, is composed of two different islands with differing orientations (highlighted by blue lines) (adapted from [52]).

figure 9 will most likely be filled by carbon atoms, which will not exhibit a clear graphitic sp^2 type coordination. Undercoordinated or overrcoordinated atoms may be possible (see in more detail in the next section).

3.4. Stability of two-dimensional amorphous carbon

It is worth having a brief look at the state-of-the-art in the field of amorphous carbon, as it may shed some light on the chances of forming amorphous or strongly disordered GBs at low growth temperatures. Bulk amorphous carbon in its various forms ranging from hydrogenated amorphous carbon (mainly sp^2 bonding) to diamond-like amorphous carbon (mainly sp^3 bonding) has been intensively investigated, both from the point of view of basic science and for practical applications [54–57]. However, a one atom thick amorphous carbon may be thought to be different from bulk amorphous carbon. Recent experimental results obtained by aberration corrected-HRTEM (ac-HRTEM) confirm that a-C is a stable structure even when it is one atom thick, and contains a significant quantity of topological defects, like observed in reduced graphene oxide. These can be further classified into isolated topological defects (pentagon–heptagon pairs), and extended (clustered) topological defects

that appear as quasi-amorphous single-layer carbon structures [58]. These extended defects predominantly incorporate a large number of carbon pentagons, heptagons and rotated hexagons in a nanometer-sized area. Nevertheless, all carbon atoms in these areas are bonded to three neighbors in a planar sp^2-configuration. The areas containing the extended defects are surrounded by crystalline graphene; this shows that these two structures can coexist as a stable structure. Another relevant observation is that the graphene regions in the vicinity of these clustered defects can be highly distorted. These distortions are typically limited to areas immediately adjacent to the defect clusters, while the larger defect-free graphene areas appear undistorted [58]. In a very recent work, the 2D amorphous carbon was produced from crystalline graphene by e-beam irradiation inside the ac-HRTEM. Using electron irradiation, an sp^2-hybridized one-atom-thick flat carbon membrane was created with a random arrangement of polygons, including four-membered carbon rings [59]. The graphene was produced by micro-mechanical cleavage and e-beam energies in the range of 80–100 keV were used for HRTEM imaging. Prolonged irradiation to a total electron dose of 1×10^{10} e^- per nm^2 at a beam energy of 100 keV yielded a coherent, single-layer membrane composed of a random patch of polygons. Holes have also formed, but only on a small fraction of the area. The Fourier transform of the image shows that the resulting structure is completely amorphous [59]. It is worth pointing out that structural model calculations and the computation of the corresponding electronic structure indicate that such clustered non-hexagonal rings may give rise to localized states in the vicinity of the Fermi level [59]. Another important finding is that bond reorientation without knocking out atoms from the lattice may occur at energies as low as 80 keV (see figure 3 in [59]). This may indicate that under the usual conditions of HRTEM investigations at around 80 keV, the amorphous GBs may recrystallize. As the displacement energy threshold of atoms in the central area of reconstructed defects is higher than that of pristine graphene by as much as 5% [60], it is very likely that the defective graphene regions under low-energy electron irradiation (about 100 keV) may tend to recrystallize in such a way that the non-hexagonal ring configuration of the lowest energy will be separating the two neighboring graphene crystals. Indeed, experimental HRTEM images show that the small, strongly disordered polygon clusters surrounded by crystalline graphene tend to reduce their size under e-beam irradiation (see figure 3 in [61]).

4. Grain boundaries in chemical vapor deposition graphene grown on solid Cu

4.1. Intragranular and intergranular grain boundaries

In the CVD growth of graphene on Cu, two distinct types of GBs may be produced: (i) GBs within grains originating from a common nucleation center; these will be called intragranular GBs; and (ii) GBs originating by growing together platelets originating from independent nucleation centers; these will be called intergranular GBs. It seems unlikely that the two kinds of GBs would have similar atomic scale structures. For example, under the conditions of 'envelope growth' described in [62], single graphene crystallites with dimension up to 0.5 mm were grown. The morphology of the edges clearly shows that the growth is dendritic, i.e. systematically the growing edges became unstable and new dendritic branches were nucleated (figure 10). In the region where the three platelets meet (upper left-hand corner in figure 10), the alteration of the morphology of the dendrites clearly indicates a reduced supply of C atoms, while the dendritic morphology indicates a growth mechanism in which individual atoms and not clusters are attached to the growing structure. Again, the growing together of such corrugated edges

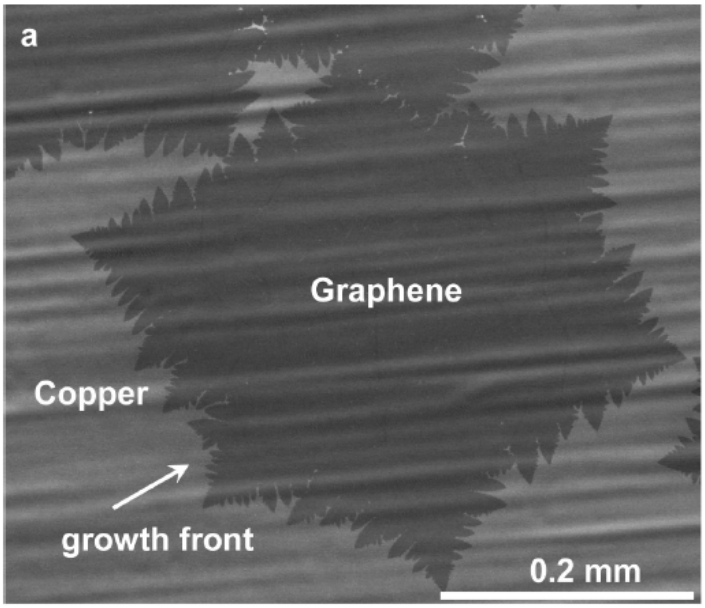

Figure 10. SEM images of graphene on copper grown by CVD, at 1035 °C at an average growth rate of $\sim 6\,\mu\mathrm{m\,min^{-1}}$ (reproduced from [62], copyright (2011) American Chemical Society). Note in the upper left corner of the image three large graphene platelets growing together and forming an almost completely closed graphene free region. The morphological deviations from the average dendritic shape in the regions where the platelets meet indicate that, as expected, in these regions the supply of C atoms is significantly lower than in the free regions of the growth front.

is unlikely to yield a regularly structured intergranular GB. The interface separating the two graphene crystallites will be closer to amorphous 2D carbon, while the intragranular GBs may have a structure closer to regular as they are produced continuously between the dendritic branches of the same graphite platelet, while the growth front advances through the addition of carbon atom by atom.

Despite the growth by atomic attachment, the different dendritic branches—belonging to different platelets originating from independent nucleation centers—when growing together will yield an irregular intragranular GB. Similar irregular intergranular GBs may be expected under those conditions for which the Smoluchowsky-type coarsening is dominant, i.e. small clusters diffusing on the surface will be attached to larger graphene platelets.

It was found by low-energy electron microscopy analysis that the large graphene platelets had a single-crystallographic orientation, with an occasional domain having two orientations [62]. However, this is not the general case, for example in the widespread, low-pressure CVD (LP-CVD) method [63], the very frequently observed four-lobed graphene platelets are, in fact, made from four crystallites originating from a common nucleation center but having a different crystallographic orientation for each lobe [64]. In platelets of this type, the intragranular GBs grown during the platelet formation may be different from the intergranular ones produced when different platelets grow together to yield a continuous film.

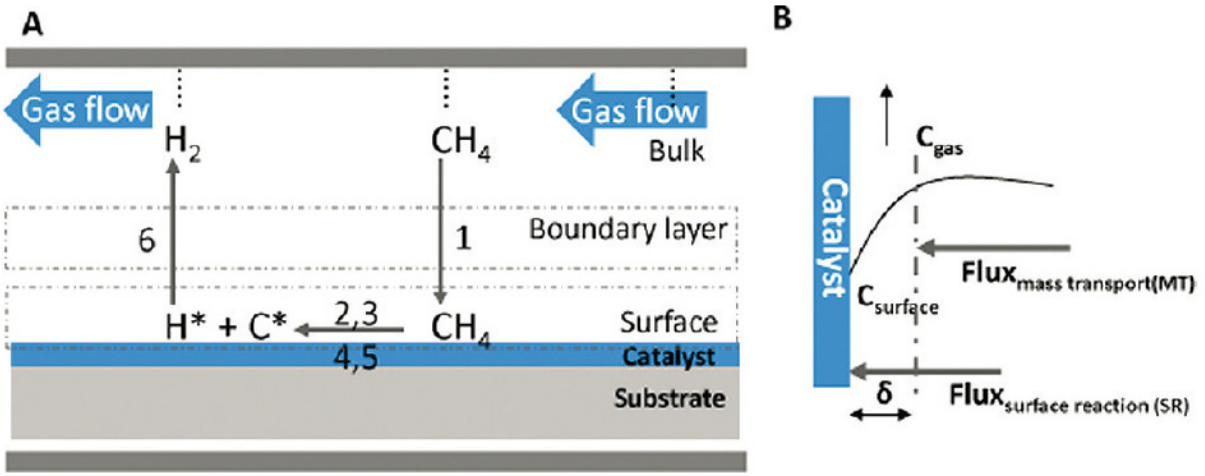

Figure 11. (A) Processes involved during graphene synthesis using low carbon solid solubility catalysts (Cu) in a CVD process. (B) Mass transport and surface reaction fluxes under steady-state conditions (reproduced from [65], copyright (2010) American Chemical Society).

4.2. Grain boundaries in low-pressure chemical vapor deposition and in ambient pressure chemical vapor deposition

The CVD growth of graphene was reviewed recently [5], so the detailed review of the CVD process is beyond the scope of the present review; however, a few characteristic points will be outlined below for the LP-CVD and for the AP-CVD of graphene.

The two different CVD processes (LP-CVD and AP-CVD) were compared recently by carrying out both processes in the same experimental setup. Although the thermodynamics of the synthesis system remains the same, based on whether the process is performed at atmospheric pressure (AP), low pressure (LP) (0.1–1 Torr) or under vacuum (10^{-4}–10^{-6} Torr) conditions, the kinetics of the growth phenomenon are different [65]. Graphene syntheses using a Cu catalyst in AP-CVD processes at higher methane concentrations revealed that the growth is not self-limiting, which is in contrast to previous observations for the LP-CVD case.

The Cu AP-CVD growth results varied from a monolayer at lower methane concentrations (parts per million concentration) to multilayer domains with a monolayer graphene background at higher methane concentrations (5–10% by volume), indicating that the growth is not self-limiting under higher methane concentrations. In accordance with previously reported data [66], the LP-CVD results confirm the large area uniformity of as-grown graphene. Representative characterization data of monolayer graphene synthesized using Cu substrate under LP-CVD conditions, in particular the density of defects based on the absence of D peak intensity in the Raman spectra, indicate a lower defect density compared to samples prepared under AP-CVD conditions [65].

LP-CVD and AP-CVD present characteristic differences in the nucleation and growth, too. The growth under AP-CVD was reported to occur with platelets of hexagonal shape possessing either zigzag or armchair edges [67], which is clearly different from the four-lobed platelets [68, 69] or the platelets with more irregular shapes [19, 62, 69, 70] occurring in LP-CVD. In the above AP-CVD growth, the morphology and perfection of geometric structure of graphene were found to be strongly dependent on CH_4 flow rates [67].

The global CVD process can be split into several elementary processes [65], as shown schematically in figure 11: the carbon species (i) diffuse through the boundary layer and reach the surface, (ii) they get adsorbed on the surface, (iii) decompose to form active carbon species, (iv) diffuse on the surface of the catalyst or into the catalyst close to the surface and form the graphene lattice, (v) inactive species (such as hydrogen) get desorbed from the surface, form molecular hydrogen, and (vi) diffuse away from the surface through the boundary layer and are eventually swept away by the bulk gas flow. Depending upon whether the processes take place in the boundary layer (1, 6) or near or closer to the surface (2–4), they can be classified into two regimes: the mass transport region, primarily involving diffusion through the boundary layer, and the surface reaction region. At high temperatures, under typical AP-CVD conditions, mass transport (diffusion) through the boundary layer is rate limiting, and under LP-CVD and vacuum conditions, the surface reaction is the rate limiting step [65]. Under AP-CVD conditions, geometric effects of the gas flow and of the geometry of the CVD chamber play a critical role in the overall synthesis. Under LP-CVD conditions, the surface reaction regime is rate limiting, and as long as the temperature is maintained uniform across the length of the Cu surface, the thickness of the graphene is uniform.

A further effect that may influence the morphology of the growing platelets, and through this the kind and number of intergranular GBs that will be formed, is the concentration of hydrogen [71, 75]. H_2 is added to the gas mixture used for CVD on purpose, and it does not originate only from methane decomposition. The catalyzed surface reaction of hydrocarbons, in fact, is an equilibrium reaction. Hydrogen was used in single-wall carbon nanotube growth to reduce the formation of amorphous carbon by etching it away. So, H_2 may influence the morphology and the edge structure of the growing platelets [71] (see figure 12) and the coarsening process, too, and by this the final defect concentration of the continuous graphene film. For example, it was found that in AP-CVD, the growth rate of graphene films is dramatically decreased with increasing H_2 concentration [71]. It was suggested in this work that the presence of H_2 leads to many intergranular GBs and wrinkles, which are responsible for the observed graphene films of low quality prepared with high H_2 concentration.

From figure 12 and the findings of [72], one may conclude that under the conditions of AP-CVD the regular hexagonal shape can be obtained when intensive hydrogen etching, exhibiting crystallographic selectivity, is stabilizing the shape by producing zigzag edges as shown by Raman mapping [71]. In contrast, under the conditions of low H_2 etching, the growth has a dendritic character. Also, the growth kinetics is very different in the regimes of low and high hydrogen partial pressures. Similar effects are reported for LP-CVD, too. In fact, hydrogen acts as a *co-catalyst* in both LP-CVD and AP-CVD in the formation of active surface bound carbon species (C_yH_x)s required for graphene growth and controls the grains shape and dimension by etching away the 'weak' carbon–carbon bonds [71].

5. Grain boundaries in chemical vapor deposition graphene grown on molten Cu

A very remarkable recent development in the CVD growth of graphene on Cu is based on the use of molten Cu instead of solid, polycrystalline Cu. The molten Cu may be supported on SiO_2, by Mo or W foil [73, 74]. One of the main advantages of using a molten catalyst is the complete elimination of previous surface history (rolling, oxidation, crystalline structure, GBs in the Cu foil, etc) and another important advantage is the elimination of the influence of Cu step formation and migration [64] during the CVD growth.

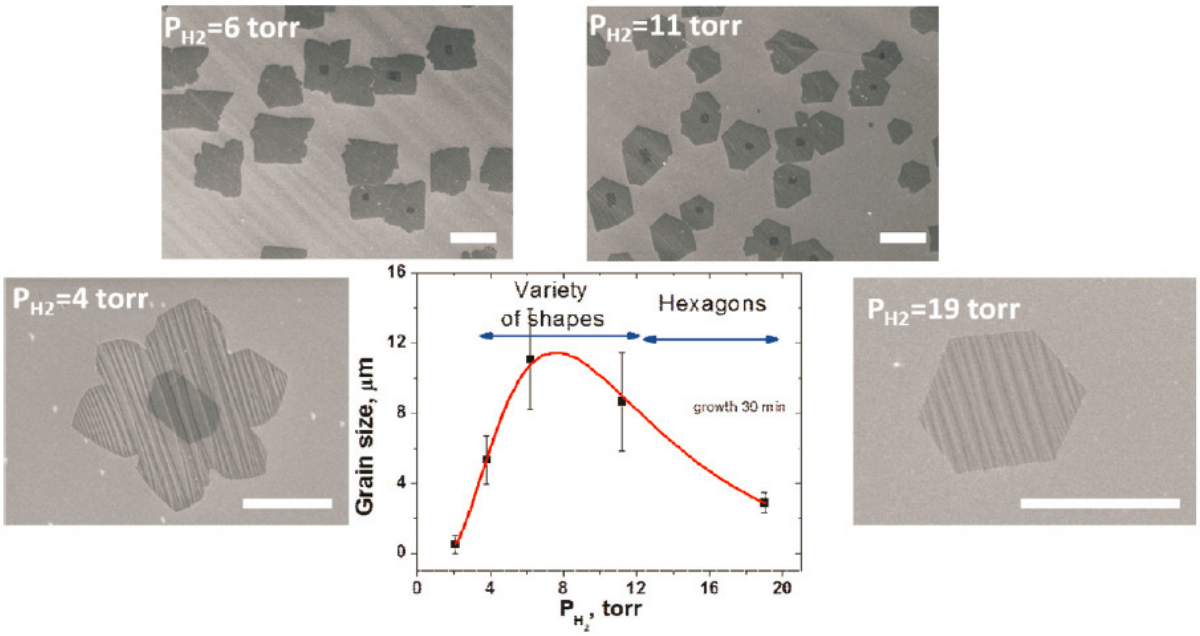

Figure 12. The average size of graphene grains grown for 30 min at 1000 °C on Cu foil using 30 ppm methane in an Ar mixture at 1 atm, as a function of partial pressure of hydrogen. The insets illustrate SEM images of the typical shapes under these different conditions. Note that perfect hexagons are observed only at higher hydrogen pressures. Irregularly shaped grains grown at low hydrogen pressure have smaller size second layers (and even third layers on some) in the centers of grains. Scale bars are 10 μm (top two images) and 3 μm (bottom two images) (reproduced from [71], copyright (2011) American Chemical Society).

In the first report on the use of molten Cu [73], unfortunately, the pressure values used are not specified. One may deduce from the previous work of the authors [67] that the growth may have been carried out in AP-CVD conditions. It was found that, typically, the hexagonal graphene flakes (HGFs) were well dispersed on the surface of the molten Cu, and there was no clear alignment relation between different HGFs when the HGFs were not fully covering the surface (figure 13(b)). When the density or coverage of HGFs on the Cu surface increased, introducing spatial constraint of the HGFs, the HGFs became self-aligned into an ordered structure with the most compact packing arrangement (figure 13(c)). The edge-to-edge alignment of HGFs led to the formation of low-angle GBs for adjacent HGFs [73]. As shown in figure 13, by controlling the nucleation and the growth rate, different degrees of ordering could be achieved. Particularly interesting is the regular structure in figure 13(d), which will introduce a very low level of disorder originating from GBs in the grown graphene layer.

The average growth rate of HGFs was estimated to be 10–50 μm min^{-1} on flat Cu/W, which is much higher than the rate of 0.1–0.2 μm min^{-1} observed for the case of HGFs grown on a Cu solid surface [67]. This shows that a liquid Cu surface allows fast growth rates. Additionally, the regular hexagonal shape indicates that the growth is subject to minimal constraints from the essentially 'structureless' liquid surface. Electrical measurements showed that the average hole mobility values in HGF devices fell into the range (1000–2500 cm^2 V^{-1} s^{-1}).

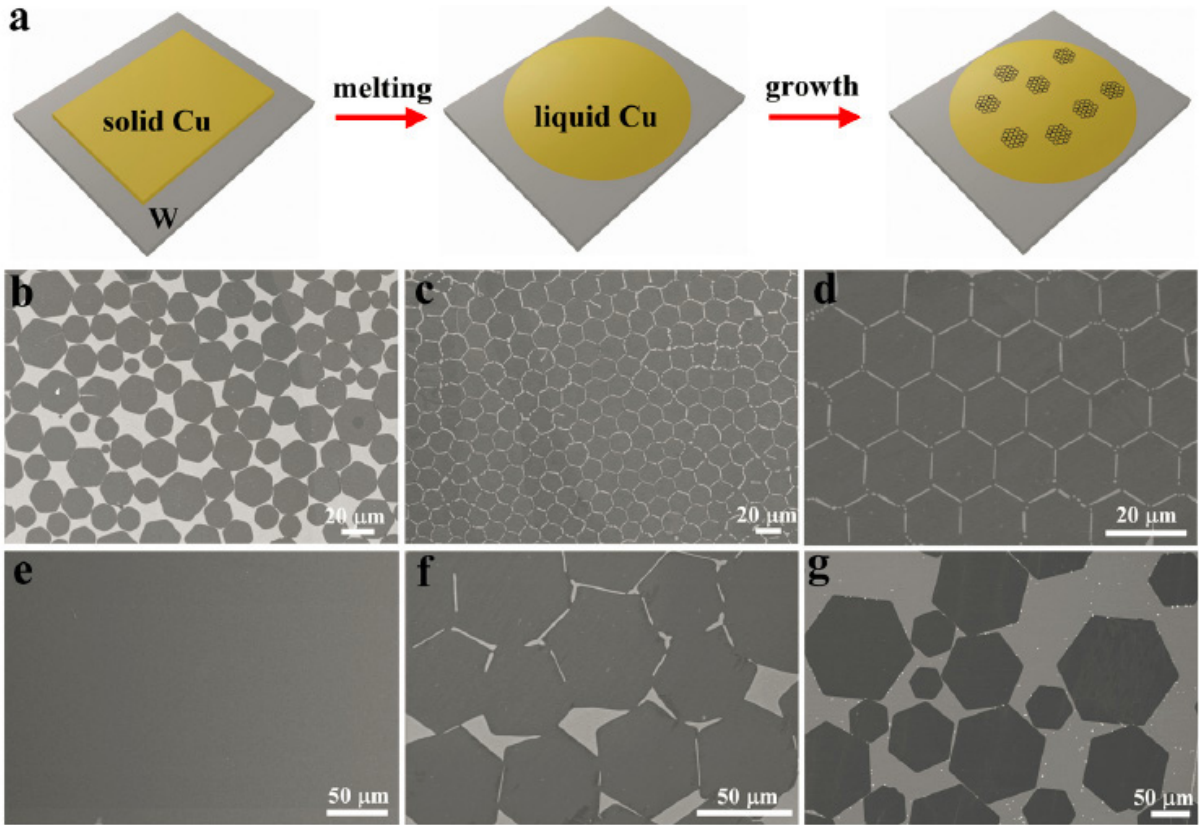

Figure 13. The growth of HGFs on flat liquid Cu surfaces on W substrates. (a) Scheme showing the CVD process for the synthesis of HGFs on a liquid Cu surface. (b) SEM image showing partially covered and well-dispersed HGFs using 6 sccm CH_4/300 sccm H_2 at 1120 °C for 30 min. (c) SEM image of HGFs showing a compact assembly of HGFs in which the dark and bright parts represent HGFs and the Cu surface, respectively. (d) SEM image of a near-perfect 2D lattice composed of similar-sized HGFs. (e) SEM image of the sample for 2 h growth showing the continuous graphene film with uniform contrast. (f) and (g) SEM images of large-sized HGFs showing that the average sizes are approximately 50 and 120 μm using 1140 and 1160 °C, respectively. Experimental conditions from (c) and (d) are the same, using 6 sccm CH_4/300 sccm H_2 at 1120 °C for 38 min (reproduced from [73], copyright (2012) National Academy of Sciences, USA).

Quite remarkably in a second recent report on CVD growth of HGFs on molten Cu (supported on Mo), no GBs or other large-scale intrinsic defects were found after an HRTEM examination of 50 individual 2 μm windows [74]. The hydrogen flow rate was varied in a gas mixture of 1 : 3 H_2/Ar at 1090 °C from 10 to 80 sccm. For growing HGFs, CH_4 (10 sccm of a 1 : 99 CH_4/Ar mixture) was added for a desired period of growth time. While at 80 sccm H_2, regular HGFs were obtained, already at 40 sccm H_2 the shape started to deviate toward a dendritic type of growth with the apexes of the hexagons growing faster than their straight edges, and at a flow rate of 10 sccm H_2 graphene platelets exhibited a completely irregular shape [74]. Electron backscatter diffraction (EBSD) indicates that after growth, the orientation of the solidified Cu surface is mainly (110). The HGFs were found to have the same orientation

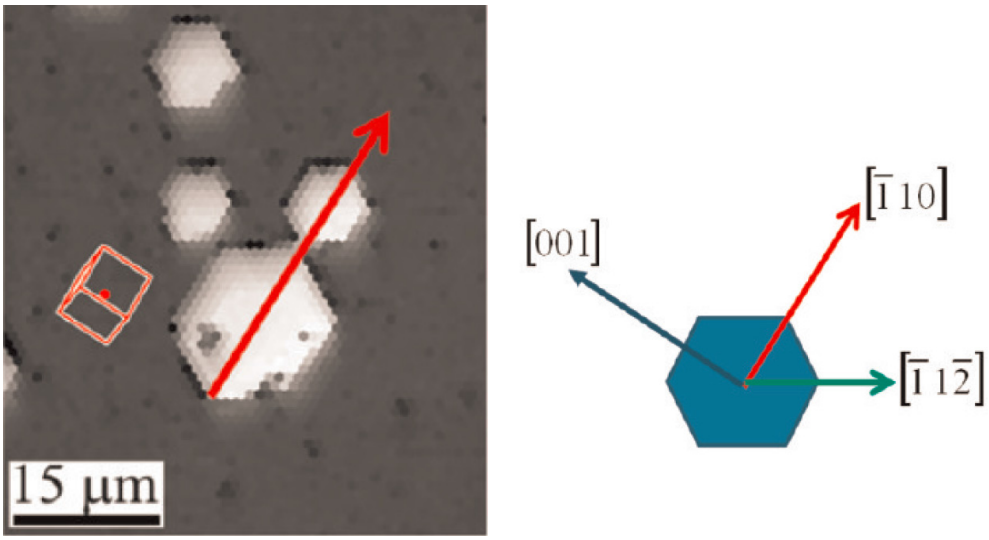

Figure 14. EBSD SEM image showing hexagonal graphene domains with a red arrow indicating a copper [$\bar{1}$ 1 0] lattice direction. The red cube shows the orientation of the underlying copper unit cell. On the right-hand side, a diagram showing the orientation of the copper lattice with respect to the hexagonal-shaped graphene domain (reproduced from [74], copyright (2012) American Chemical Society).

on the Cu (110) face with a deviation of 0.8° on average (figure 14) [74]. Detailed selected area electron diffraction of the continuous graphene film showed an angular misorientation smaller than 2° over a distance of 81 μm.

The combination of high levels of hydrogen flow in AP-CVD with molten Cu may be extremely promising for a dramatic reduction of structural disorder originating from randomly nucleated and randomly oriented graphene platelets growing together. A very important advantage of the liquid catalytic surface is that, in contrast to the solid surfaces, including the single-crystalline ones such as Cu(111) [75–77] or Cu(100) [76, 78], it stays atomically smooth under the growth conditions for HGFs. Furthermore, the molten surface avoids large physisorption strains reported on Cu [79]. Moreover, large-area molten metal surfaces are much cheaper to produce than large-area single-crystalline metallic foils.

In summary: from the point of view of GB structure the use of molten Cu substrate is the most advantageous choice as it allows the use of higher growth temperatures; it eliminates all disturbing factors originating from the previous history of the Cu surface, it does not show step formation during the growth of graphene and it allows for the control of the orientation of neighboring graphene platelets (see figure 13(d)), which will reduce the amount of disorder 'frozen in' in the GBs.

6. Experimental atomic scale structure of grain boundaries by high-resolution transmission electron microscope, scanning transmission electron microscopy and scanning probe microscopy

In the discussion above, the most frequently used experimental results were produced by electron microscopy and scanning probe (STM and AFM) microscopy. It is clear that the

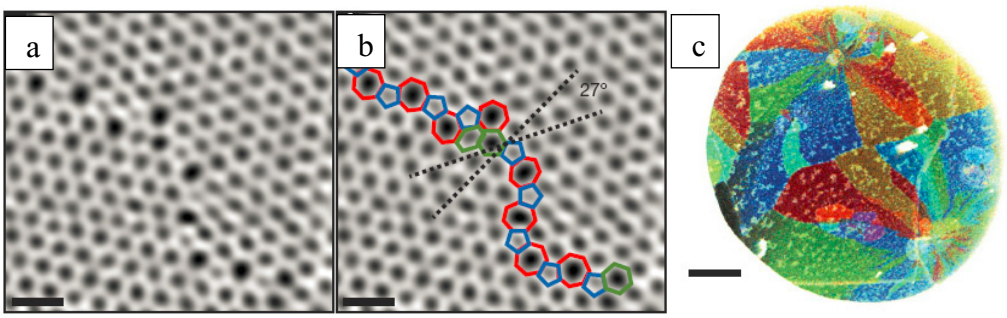

Figure 15. (a) Two grains (bottom left, top right) in CVD graphene intersect with a 27° relative rotation. An aperiodic line of defects stitches the two grains together. (b) The image from (a) with the pentagons (blue), heptagons (red) and distorted hexagons (green) of the grain boundary outlined. Panels (a) and (b) were low-pass-filtered to remove noise; scale bars: 0.5 nm. (c) Placing an aperture in the diffraction plane from a polycrystalline area filters the scattered electrons forming a corresponding dark-field image showing the real-space shape of these grains; using several different aperture locations and color-coding them produces a false-color, dark-field image overlay depicting the shapes and lattice orientations of several grains (reproduced by permission from Macmillan Publishers Ltd: Nature [80] copyright (2011)).

microscopic data are extremely important in studying and understanding the GBs. In revealing the details of the atomic structure of the GBs, HRTEM [61], scanning TEM (STEM) [80, 81] and STM [32, 45, 82–84] are the most effective, while the local electronic structure of the GBs may be investigated by STS [45, 82]. STM/STS has several advantages as compared to HRTEM and STEM: (i) the GBs can be examined without any further manipulation on the metallic surface where they were produced; (ii) under normal imaging conditions, the GBs are not altered by STM and STS investigations; (iii) as shown for example by figure 9, under certain circumstances the GB formation process can be investigated *in situ*; and (iv) the local electronic structure can be studied and compared to that in the bulk of the graphene platelets separated by the GB. On the other hand, in contrast to STEM, the exact atomic arrangement within defects most often cannot be revealed directly by STM; it can only be inferred from model calculations [15, 16, 32].

A detailed GB study using HRTEM revealed that under the conditions of e-beam irradiation, GBs are predominantly constructed of continuous chains of pentagon–heptagon pairs and the GBs tend to take on meandering, locally curved configurations [61]. Movies taken on the GB evolution in the electron microscope convincingly show that once such a configuration is attained, its general structure and shape will be conserved despite the continuous transformations between several, essentially equivalent configurations. This is attributed to the fact that significant changes in the atomic structure of graphene can be induced via bond rotations under 80 kV electron irradiation, as shown previously [59], while knock-on sputtering of three-coordinated carbon atoms becomes significant only at slightly higher acceleration voltages.

Atomic resolution images of a GB in CVD graphene were obtained by annular dark field STEM (ADF-STEM) at a beam energy of 60 keV, with an electron probe size close to 0.13 nm (figure 15). The dark field TEM images acquired on the CVD graphene revealed that the

material is polycrystalline with an average grain size of 250 nm with the most abundant grain size being in the range of 100 nm. The grains have complex shapes and many different crystal orientations [80].

The reciprocal misorientation of neighboring grains was found to cover the full angular range of 0–30°, with a somewhat more frequent occurrence of small-angle GBs (∼10°) and large-angle GBs (∼30°). By comparing three different CVD methods: methods A and B, two furnace-based CVD methods differing only in the purity of the Cu foil used, and method C that used a rapid thermal processor tube furnace, it was found that the growth conditions may have a dramatic effect on the grain size [80]. The slight differences between growth methods effected significant changes in the grain size, shape and crystallographic orientation of the CVD graphene. For example, with growth method C, grains averaging 1–4 μm were obtained, which is an order of magnitude larger than the grains grown using method A (shown in figure 15).

Very similar results were obtained by using CVD graphene [19] transferred to freshly cleaved mica substrates and subjected to mild oxidation in air at 500 °C. The GBs were revealed by the oxidation, while structurally perfect regions were unaffected as checked by the parallel oxidation of micromechanically cleaved graphene under identical conditions [85]. By taking atomic resolution AFM images within each grain, it is possible to characterize the misorientation of neighboring grains. The false color grain misorientation map and the corresponding grain size and misorientation statistics are shown in figure 16.

None of the above presented methods provides information on the 3D structure of the GBs. For example, the apparently planar GB in figure 15 was calculated to have, in fact, a 3D structure [86], as revealed by figure 17. This 3D structure was obtained by total energy minimization based on a classical Brenner–Tersoff-type interatomic potential, the edges of the structure being passivated with H.

Indeed, topographic STM images confirm that GBs usually have 3D structure [82–84]. On the other hand, when the defect is just a linear and periodic chain of non-hexagonal rings, separating two identically oriented graphene regions, surprisingly, the structure may be practically flat [32]. For this particular defect configuration, composed of octagons and pentagons, the computation of the density of states shows states localized at the Fermi energy. Comparing this finding with the statistics of GB-related localized states of [45], one may conclude that this type of GB may be relatively rare.

Beyond topography, STM can reveal several other important parameters such as conductivity, electronic structure and doping [82] (figure 18). It was found that the conductivity within the grain boundary is about an order of magnitude lower compared to the defect-free graphene lattice. This implies that from the electrical point of view, the interconnected GB network divides the graphene sample into highly conductive single-crystalline islands delimited by more resistive interface regions of a few (3–5) nanometers width. These findings are in agreement with transport measurements reporting that the inter-grain conductivity (across a GB) was found to be reduced by approximately an order of magnitude as compared to the intra-grain conductivity (no GB), when transport through purposefully produced, individual GBs, was measured [87, 88]. The GBs of CVD graphene form n-doped inversion channels within the overall p-doped graphene lattice [82]. The origin of this phenomenon can be attributed to the self-doping, whereupon a charge transfer occurs between the defect-free graphene lattice and the non-hexagonal carbon rings making up the grain boundary. An additional source of doping could come from functional groups or adsorbates, which preferentially attach to the defective GBs; this will be discussed in more detail in section 8.

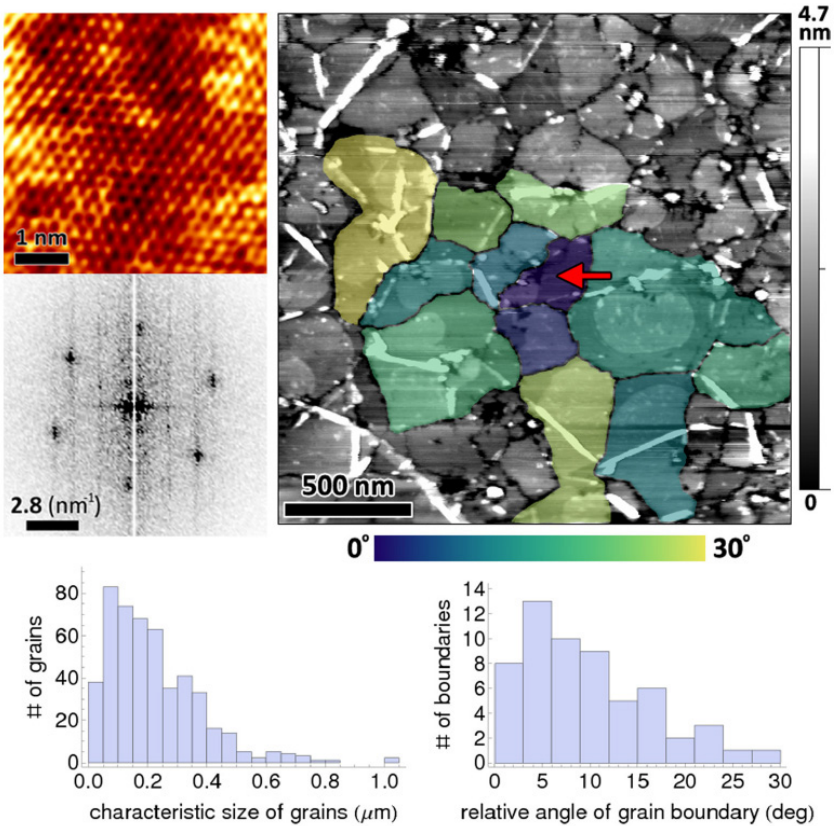

Figure 16. AFM image of CVD graphene showing the etch trenches. By comparing the Fourier transform of atomic resolution AFM images of individual grains, one can make a false color map of the crystallographic orientation of the grains relative to a given direction. Two small images to the left show one such atomic resolution image and the Fourier transform thereof. The atomic resolution image was recorded by contact mode AFM on the grain shown by the red arrow. Histograms at the bottom show the distribution of the grain size (left) and the relative angle of the grains forming the boundaries (right) (reprinted with permission from [85], copyright 2011, American Institute of Physics).

STM and STS measurements carried out in ultra-high vacuum on graphene grown on Cu(111) at 1000 °C revealed that, despite the single-crystalline nature of the substrate, the synthesis on Cu(111) involves the nucleation of monolayer islands of graphene that patch together like a quilt to form larger single-layer sheets; as a result there are numerous domain boundaries that scatter electrons and can affect carrier mobility. The overall interaction between the graphene and Cu(111) substrate results in the observation of two predominant moiré patterns [83]. The growth cycle, including cooling to room temperature under ethylene followed by flashing to 1000 °C, was somewhat different from the conventional CVD graphene synthesis: it resembled more an atomic layer deposition than traditional CVD growth. Four thermal cycles resulted in 0.35 monolayer of graphene and eight thermal cycles resulted in 0.8 monolayer of graphene [83]. The graphene platelets are clearly resolved through STS (figure 19); the contrast between the graphene and the Cu(111) within the 2D conductance map indicates a difference

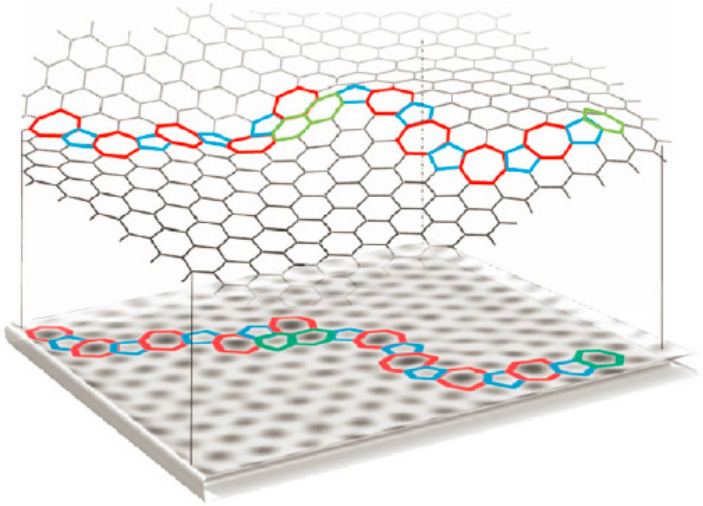

Figure 17. Pentagons (blue) and heptagons (red) in a grain boundary should result in noticeable off-plane 3D landscapes, obtained here by computational relaxation, for an example based on aberration-corrected ADF-STEM image [80] (bottom) (reproduced from [86], copyright (2011) American Chemical Society).

in the electronic structure at the particular energy of $U_b = -200$ mV. The different grains are revealed by the moiré-type patterns that are formed by overlaying the hexagonal graphene with the Cu(111) (figure 19). The nucleation and growth of individual platelets, which are mobile at elevated temperature, take place. Platelets stitch together with other platelets to form larger sheets, resulting in different domains and domain boundaries. This is not initially apparent in the topographic data but is clearly observed with STS. The observation of multiple moiré patterns, which results from different rotational alignments of the graphene lattice (2.46 Å) with the underlying Cu(111) lattice (2.56 Å), indicates that the graphene is weakly coupled to the substrate [83]. Like in the case of the graphene growth on Ir(111) discussed above, the moiré patterns are very useful in revealing differences in the orientations of the grains, which otherwise would not be visible in larger scale images. Electron scattering patterns are clearly visible in the region of GB in figure 19(b) and the GB is clearly of 3D character. No atomic resolution is observed in the region of the GB, but various superstructures originating from the scattering of electrons on the non-hexagonal rings in the region of the GB are present.

In fact, the GB seen in figure 19(b) shows many similarities with the GB formed in the FLG grown on 6H-SiC (figure 7). Both GBs exhibit accidentally alternating 'hills' and 'valleys' along a randomly curved line. On both sides of the GB, complex patterns formed by electron scattering are seen. They make it difficult to estimate at each point the true width of the GB, i.e. the region in which the atomic structure deviates from the perfect honeycomb network, but on average the extension of the perturbed region can be considered to be rather of nanometer order than of 0.1 nm order.

The topographic STM and STS data on the structure of the GBs in CVD graphene discussed above are in full agreement with recent structural simulations of polycrystalline graphene (see figure 1 in [21] and section 2 of this paper), in which the GBs in fact have an amorphous character [59]. The observation that the electronic structure in the STS mapping does not depend on the orientation of the graphene grains—see, for example, the similar contrast of graphene

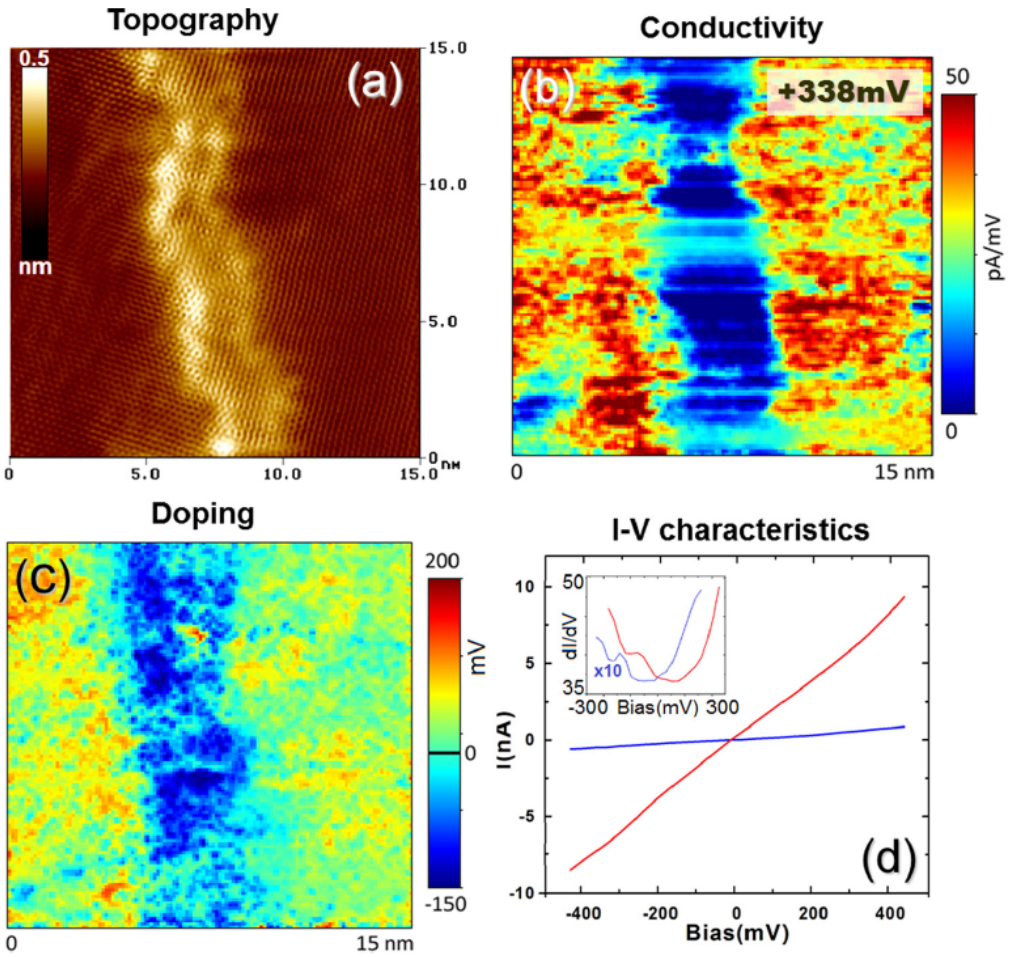

Figure 18. Atomic resolution constant-current topographic STM image (100 mV, 1 nA) of a 29° graphene grain boundary, with the boundary region displaying a bright contrast. (b) Spatially resolved tunneling conductivity map revealing a markedly suppressed conductivity at the grain boundary region. (c) Spatial map of the Dirac point (minimum of dI/dV) position relative to the Fermi energy, indicating the local doping. (d) Representative individual current–voltage characteristics acquired at the grain boundary (low, blue) and over the unperturbed graphene lattice (steep, red). The corresponding numerical derivatives (differential conductance) are shown in the inset (reproduced with permission from [82], copyright 2012, American Institute of Physics).

platelets with different orientations to the single-crystalline Cu background in figure 19(a)—and recent findings that the characteristics of individual GBs (lower conductivity and n-type doping as compared with the bulk of the graphene platelets) investigated by STS do not depend on the particular misorientation between the neighboring gains [82] also suggest that in fact the structure of the GBs in CVD graphene on Cu may have a strongly disordered (amorphous) character in the as-grown state; as a consequence, the particular orientation of the grains on the two sides of the GB has a smaller contribution to the electronic structure of the GB.

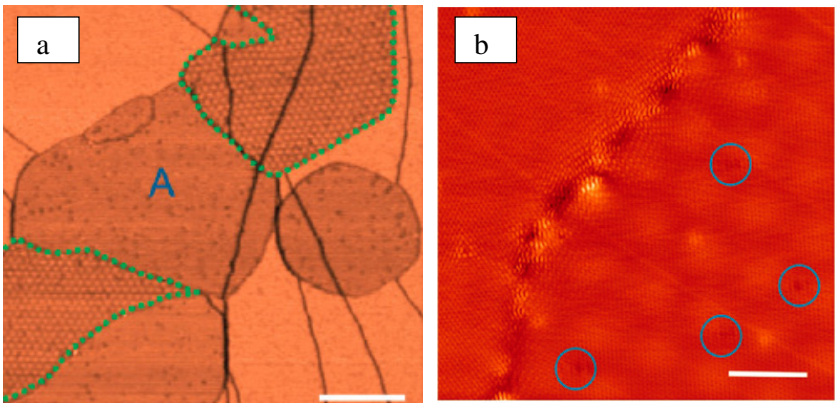

Figure 19. (a) STM differential conductance $\mathrm{d}I/\mathrm{d}V$ images of graphene islands on Cu(111) ($U_\mathrm{b} = -200\,\mathrm{mV}$). The $\mathrm{d}I/\mathrm{d}V$ signal can differentiate graphene from the copper surface. Graphene shows dark contrast in this image. The areas highlighted with dotted lines are graphene domains showing moiré patterns. Scale bar: 200 nm. (b) Topographic atomic resolution STM image at a domain boundary, showing the honeycomb structure of graphene. The moiré pattern in the upper left domain cannot be observed under this scanning condition. The periodicity of the moiré pattern in the lower right domain is ∼3.0 nm. Electron scattering is clearly observed in the region of the GB. Scale bar: 4 nm. Some adsorbates on the graphene surface are highlighted with blue circles (reproduced from [83], copyright (2010) American Chemical Society).

7. Transport across GBs

7.1. Electric transport

Graphene poly-platelets are very interesting from the point of view of basic science, as for the first time, GBs and their behavior may be investigated in 2D systems by HRTEM and STEM. On the other hand, the existence and the properties of GBs are of extreme importance for practical applications of graphene. Beyond their influence on the mechanical properties—which is not within the scope of the present review—they may have dramatic effects on the transport properties, too [33, 37, 89, 90]. For example, first-principles quantum transport calculations showed that in the case of periodic GBs, depending on the GB structure two distinct types of transport behavior can be found—either high transparency or perfect reflection of charge carriers over remarkably large energy ranges [90]. Certain special structures such as the so-called 558 line defect [32] may even exhibit important and attractive properties such as valley filtering [91].

Conductive-tip AFM measurements carried out over large enough areas to cross several GBs indicated that the GBs do not have significantly higher resistivity than the graphene platelets. An upper limit was estimated for the resistivity of the GBs of $R_\mathrm{GB} < 60\,\Omega\,\mu\mathrm{m}^{-1}$, where L is the length of the grain boundary, to be compared with the sheet resistivity of $R_\mathrm{graphene} = 700\,\Omega\,\mathrm{per}\square$ for the entire device. In other words, the resistance of the GBs is less than one-third the resistance of a 250 nm grain [80]. In contrast, in purposefully created GBs between mainly zigzag edged graphene grains grown by AP-CVD on Cu [87], it was found

by Raman mapping that, in the region where the two grains merged, the D band intensity was increased significantly as compared to the bulk of the grains (see figure 4(d) in [32]).

Electrical transport measurements were carried out on multi-terminal devices fabricated from graphene grains transferred onto SiO_2/Si wafers. All the *I–V* curves measured at room temperature, both across the GB and within one single grain, for two coalesced graphene grains that meet at a single grain boundary, exhibited an ohmic character. The resistances extracted from the slopes of these *I–V* curves were $R_L = 550\,\Omega$ (left grain), $R_R = 200\,\Omega$ (right grain) and $R_{CG} = 3\,k\Omega$ (across the grain boundary), respectively [32]. This shows that the resistivity across the GB is significantly higher than within the grains. This result is consistent with STM and STS data reported in [82]. Low-temperature magnetotransport measurements showed weak localization (WL) effects in the region of the GB, while the intragrain WL was found to be negligible. This shows that GBs are a major source of intervalley scattering in graphene devices (where the inter-grain current has to cross the grain boundary), whereas such a scattering is less significant within the single-crystal graphene grains [32]. GB scattering effects were evidenced in epitaxial graphene grown at 1800 °C on 4H-SiC, too [92].

In a recent report on electric transport through the GBs of CVD grown polycrystalline graphene, it was unexpectedly found that the electrical conductance may improve by one order of magnitude for GBs with better interdomain connectivity [93]. The grain structure of CVD graphene was first imaged using TEM and individual domains and GBs were then addressed electrically in polycrystalline graphene. Such an approach was found to be crucial, because graphene domain structures generated during synthesis form non-trivial patterns that are strongly dependent on the growth conditions and difficult to predict *a priori* [93]. Three different CVD methods were used: (i) method A yielded grain size $D \approx 1\,\mu m$ and an irregular polygonal shape with good stitching between the grains; (ii) method B yielded $D \approx 10\,\mu m$ and grains of more regular polygonal shapes, with good stitching; (iii) whereas growth C yielded large, four-lobed, flower-like grains with $D \approx 50\,\mu m$ and frequent stitching defects. For an A type GB it was found that R_{L-R} (measured through the grain boundary between the left and the right grains) exhibited an increased resistance, particularly at gate biases near V_{Dirac}, that was attributed to additional scattering caused by the GB. The results of the measurement were interpreted to describe the presence of a GB as simply an extension of the conductance channel defined by an effective length λ associated with the GB. Different electrical behavior was observed for analogous measurements at a GB from growth C: R_{L-R} was considerably greater at all gate values than the values within individual grains, signifying increased scattering at the GB. The GB resistivity was about an order of magnitude more than that found for growth A. The mean λ value for A samples was 110 nm (five devices), and it was 880 nm for C samples (six devices). The results of TEM and transport measurements on individual GBs in CVD graphene show that the conductance of GBs is highly correlated with their structure [93]. These experimental data strongly support that the character of the GB regular versus irregular has a major influence on the electric transport across the GB. In other words, if no proper ways are found which will allow precise control of the formation and structure of the GBs, their presence may be a serious impediment to practical applications using CVD grown graphene.

Taking into account that the A type CVD process discussed above (high reactant flow rates, at ≈2 Torr pressure, 1000 °C) carried out with extreme care to avoid any contaminant yielded a field-effect mobility of 25 000 $cm^2\,V\,s^{-1}$ and a sheet resistance of ≈1 kΩ at a relatively low carrier density ($\sim 3 \times 10^{11}\,cm^{-2}$) comparable to that of exfoliated supported graphene [93], and

keeping in mind the possibilities offered by the CVD process on molten Cu [73, 74] (see, e.g., figure 13(d)), one can conclude that the proper stitching of graphene grains over large areas may soon yield a material suitable for nanoelectronic applications.

7.2. Thermal transport

To date, relatively little is know about the thermal transport across GBs in polycrystalline graphene. Theoretical calculations predict two distinct temperature ranges, below and above T^*, a crossover temperature at low temperatures. $T^* \approx T_o/2$, where T_o is governed by the dominant phonon mode [94]. Above T^* the thermal conductivity behaves like T^2, while below T^* the behavior is acutely sensitive to T_{GB}, it behaves like T^α, where α values range from 1 to 2 with increasing T_{GB}. In turn, T_{GB} depends distinctly on the packing coefficient (grain size) and GBs' angle. It should also be mentioned that T_o characterizes the temperature when the wavelength of an incident phonon becomes comparable with the size of the GB. T_{GB} decreases with an increase of the packing coefficient, the misorientation angle and/or sample size, while T_o depends on the grain boundary length only [94]. Using non-equilibrium molecular dynamics simulations, it was shown that the boundary conductance on the tilt GBs are in the range 1.5×10^{10}–$4.5 \times 10^{10}\,\mathrm{W\,m^{-2}\,K^{-1}}$, which is significantly higher than that of any other thermoelectric interfaces reported in the literature [95]. A critical grain size of $0.1\,\mu$m was identified, below which the contribution of the tilt boundaries to the conductivity becomes comparable with that of the contribution from the grains themselves.

The thermal conductivity of supported, exfoliated graphene at room temperature was found to be in the range 4.84×10^3–$5.30 \times 10^3\,\mathrm{W\,mK^{-1}}$ [96]. This unusually high value, exceeding that of bulk graphite, is related to the long phonon mean free path of graphene, which is calculated to be around 750 nm at room temperature [97]. Much lower values were found for CVD graphene on SiO_2, $\sim 400\,\mathrm{W\,mK^{-1}}$ at room temperature; the values obtained for suspended CVD graphene were found to be in the range of $2500\,\mathrm{W\,mK^{-1}}$ at room temperature [98]. When comparing suspended exfoliated graphene (3000–5000 $\mathrm{W\,mK^{-1}}$), with supported exfoliated graphene ($600\,\mathrm{W\,mK^{-1}}$), a large difference was found in thermal conductivity, which is attributed to backside scattering and the flexural phonons' leakage into the substrate [99]. Comparing the above figures for exfoliated and CVD grown graphene the difference does not appear very significant. In a recent report, the effect of the thermal properties was investigated as a function of the disorder. The characteristic size of well-ordered domains, L_a, was chosen as the parameter and the thermal conductivity of CVD graphene was investigated as a function of L_a [100]. L_a was determined from the intensity ratio of the G and D peaks in Raman spectra [101]. The thermal conductivity, K, measured on the CVD graphene samples suspended on silicon pillars appears to have a dependence on L_a, close to $K \sim L_a^{1/3}$. Despite the progressively increasing structural disorder in graphene grown at lower temperatures, it shows remarkably high thermal conductivity (100–1000 $\mathrm{W\,mK^{-1}}$) [100].

A more detailed review dedicated to the thermal properties of various nanocarbons, including graphene, can be found in the paper by Balandin [102].

8. Chemical properties of the grain boundaries

The structural differences encountered in the region of the GBs—irrespective of whether these are only non-hexagonal rings or are more complex, possibly more disordered structures—are

most probably associated with differences in the local chemical properties of the graphene layer [30]. It was found by model calculations that the H adsorption energy increases as the rings deviate from hexagons, the largest adsorption energy of $\varepsilon_i > -7$ eV [30] being found for dangling bonds. These results are in agreement with *ab initio* calculations reported recently on H adsorption on non-hexagonal rings in graphene GB regions [103]. Computed STM images of GBs after H adsorption indicate that the H atoms will be localized on the non-hexagonal rings and will appear as tunneling current maxima in the STM images. The density of states for H/GB(5–8) indicates that the electronic states along the C–H bond are mostly localized between 2 and 3 eV below the Fermi level, while in H/GB1(5–7), the electronic states of H adatoms (mostly) lie at $E_F \pm 0.3$ eV. H/GB(5–8) and H/GB1(5–7), respectively, designate a hydrogen attached to a pentagon–octagon–pentagon complex and a hydrogen attached to a pentagon–heptagon pair in the hexagonal network. As already discussed above, H is present in all CVD processes and has a significant influence on the morphology of the graphene platelets [71] and the ways in which these platelets will grow together to form a continuous film [93].

The energetics and electronic properties of substitutional B (BC) and N (NC) doping, and BN codoping in graphene with distinct grain boundary defects were investigated by *ab initio* simulations. The results indicate that a single B or N impurity atom and an isolated BN pair prefer to incorporate into the grain boundary region [104]. The calculated electronic properties show that the incorporation of a single substitutional B (N) atom produces a p-type (n-type) doping in all investigated GB structures. However, the BN codoping introduces only small modifications of the host electronic structure.

Recent statistical data on devices prepared from CVD graphene grown on Cu and transferred to SiO_2 substrates subjected to various treatments after transfer—aimed at reducing the water trapped between the SiO_2 and the graphene layer—indicated that indeed the trapped water can significantly degrade the electric parameters of such devices [105]. Using exfoliated (kish) graphene it was shown experimentally that dry oxygen and the wet ambient dope graphene in different ways on an SiO_2 substrate. Dry oxygen dopes graphene from the basal plane, while the ambient dopes graphene from the edges or from the substrate in the vicinity of the edge. Upon vacuum annealing, doping is fully reversible in the former case and is only partially reversible in the latter case. This shows that oxygen and moisture are the primary species in the atmosphere responsible for doping graphene and the defects—the edge regions or the GBs—have a marked effect on graphene doping [106].

In a recent study of the adsorption and reactions of water, oxygen, hydrogen and ammonia on epitaxial graphene grown in an UHV apparatus on Ru and Cu substrates investigated by STM, it was found on Ru(0001) that graphene line defects are extremely fragile toward chemical attack by water, which splits the graphene film into numerous fragments at temperatures as low as $-183\,^{\circ}$C, followed by water intercalation under the graphene. On Cu(111), water can also split graphene but far less effectively, indicating that the chemical nature of the substrate strongly affects the reactivity of the C–C bonds in epitaxial graphene. Interestingly, no such effects were observed with other molecules, including oxygen, hydrogen and ammonia [27]. The cleanness of the surface prior to graphene growth was confirmed by Auger electron spectroscopy and STM. Epitaxial graphene on Ru was prepared by exposing the Ru sample to ethylene at $957\,^{\circ}$C (2×10^{-7} Torr, 2 min). Epitaxial graphene on Cu(111) was prepared through exposure to ethylene at $1000\,^{\circ}$C (4×10^{-4} Torr, 15 min). The samples were then slowly

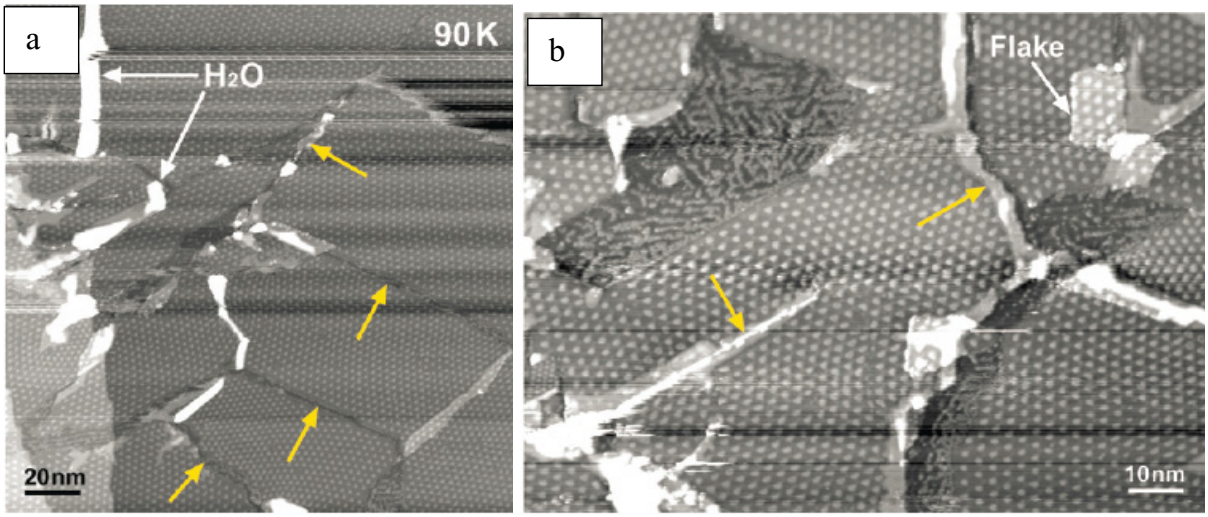

Figure 20. STM images of the graphene surface on Ru after water exposure. (a) Graphene splits into fragments along line defects, opening gaps between them, as indicated by arrows. The bright stripes are attributed to water. (b) Graphene flakes detached from the substrate moved on top of the first overlayer. Exposed areas of Ru substrate decorated with water stripes are visible. Decoupled graphene (no moiré pattern) due to water intercalation is observed along the edges of the split fragments, as indicated by the yellow arrows (reproduced from [27], copyright (2012) American Chemical Society).

cooled down and transferred to the STM in a connected UHV chamber without breaking the UHV conditions. The graphene-covered surface was exposed to submonolayer amounts of water (2×10^{-10} Torr, $\sim$1 min) at $-196\,^{\circ}$C. The adsorbed water formed clusters, indicating poor wetting of graphene. Annealing the Ru sample to $-183\,^{\circ}$C for 5 min produced notable changes, as shown in figures 2(b)–(d) of [27]. Water stripes are observed decorating some of the dislocation lines. In many areas, the graphene film appears to be split into fragments separated by gaps (figure 20(a)). The different orientations of the moiré pattern in the fragments on each side of the gaps indicate that an edge dislocation or grain boundary was previously there. In addition to the splitting, graphene fragments were found detached and displaced away from the Ru substrate, forming flakes on top of other graphene areas, as shown in figure 20(b) [27].

Similar experiments on graphene grown on Cu(111) showed that after water exposure at $-196\,^{\circ}$C, water clusters are observed on the surface, similar to the case of graphene on Ru. Subsequent annealing to temperatures below $-123\,^{\circ}$C did not produce significant effects. However, after annealing to $-123\,^{\circ}$C for 15 min, some graphene fragments were found to split from the film and displace to other locations. In contrast to the Ru case, the graphene splitting was found only occasionally on the Cu surface (about 1% area of the graphene film), indicating, here too, that the chemical nature of the substrate strongly affects the reactivity of the C–C bonds in epitaxial graphene [27]. Still these experimental results, in agreement with the findings reported in [107], indicate that at room temperature and under ambient conditions the GBs of graphene grown on Cu may be significantly affected by moisture.

9. Chemical treatment and optical characterization of grain boundaries

The above detailed chemical sensitivity of the GBs offers a handy way to combine chemical reactions of the Cu substrate and optical microscopy to quickly reveal over large areas the distribution of the GBs [107]. However, one should be aware that in this way no atomic scale information is obtained on the structure of the GBs, only their location can be revealed by oxidizing the underlying Cu. The GBs will appear as protrusions due to the formation of copper oxide underneath the graphene layer. The oxidation process takes place by selectively oxidizing the underlying copper foil through graphene GBs functionalized with O and OH radicals generated by ultraviolet irradiation under moisture-rich ambient conditions [107]. The GBs are very narrow for optical microscopy, but the width of the oxidized copper foil beneath the defective GBs is increased by the continuous supply of oxidizing radicals through the grain boundary. In addition, oxidized copper occupies a larger volume than copper, thereby allowing the visualization of the GBs using an optical microscope. The sheet resistance of large-area graphene decreased as the graphene grain sizes increased, but no strong correlation with the grain size of the copper was revealed.

10. Mechanical strength of grain boundaries

Direct experimental data on the strength of the GBs are lacking. Even the modeling results are somewhat contradictory. Using atomistic calculations, it was found that graphene sheets with large-angle GBs that have a high density of defects are as strong as the pristine material and, unexpectedly, are much stronger than those with low-angle GBs having fewer defects [108]. This trend is attributed to the critical bonds in the strained seven-membered carbon rings that lead to failure; the large-angle boundaries are stronger because they are able to better accommodate these strained rings [108]. More recently, first-principles calculations and empirical molecular dynamics simulations were used to reveal the mechanical properties of regular and periodic GBs under tensile strains. No simple correlation was found between the intrinsic strength and misorientation angle of the GBs. Instead, the intrinsic strength of a graphene GB depends on its inflection angle, i.e. on the angle the graphene sheets on the two sides of the GB make with each other. The strength decreases linearly with increasing inflection angle. It was found that GBs with high thermodynamic stability can be nearly as strong as pristine graphene, while the inflected GBs have a significantly reduced intrinsic strength due to buckling along the GBs [109]. Experimental investigation of tear formation in CVD graphene membranes (grown on Cu) inside the TEM revealed the crystallographic orientations of tears. Edges from mechanically induced ripping exhibit straight lines and are predominantly aligned in the armchair or zigzag directions of the graphene lattice. Surprisingly, tears do not follow but cross GBs [110]. The above findings indicate that further studies are needed in this controversial field.

11. Summary and outlook

The review of the literature on GBs in graphene and, in particular, on CVD grown graphene on Cu emphasizes that the formation and structure of the GBs depend on numerous conditions related to the growth process, such as growth temperature, the pressure range used (low or ambient pressure), hydrogen concentration in the growing environment, and the random

or organized arrangement of the graphene platelets with respect to each other. This last parameter will determine the way in which the stitching of the graphene platelets will take place, which in turn will impact on the electric properties of the GBs, a more disordered GB corresponding to a more significant increase in resistivity and, as shown by several STM images and magnetotransport measurements, increased scattering of the charge carriers in the region of the GB. The number of GBs is primarily related to the number of nucleation centers from which the growth starts, while the dendritic or smooth character of the edge of growing crystallites is governed by the hydrogen concentration. The dominant grain coarsening process also impacts significantly the character of the formed GBs. The number of growth parameters is far too large to allow a simple and widely applicable generalization. Nevertheless, the above enumerated factors which influence the kind of GBs formed are worth keeping in mind for a more systematic examination targeting the correlation of a certain growth parameter with the typical structure of the formed GBs and the effects of these GBs on the transport processes occurring through them. One may formulate this in a more condensed way, quoting a statement from the paper of Malola *et al* [30]: 'Grain boundaries, on the contrary, are like snowflakes—there is no flake like another, but it is enough to know that they are roughly hexagonal, flat, small and cold', which beyond its poetic phrasing also contains a significant amount of wisdom.

Despite numerous HRTEM and STEM images on GBs composed of regular (irregular) arrangements of a chain of non-hexagonal rings separating two perfectly crystalline graphene regions, the existence of amorphous GBs cannot be ruled out. Both experimental STM and AFM images, and to some extent, structural models of GBs support this possibility. The properties of these amorphous GBs, opposite to chains of non-hexagonal rings, should not depend on the particular misorientation between the two crystalline graphene regions separated by the GB. They can be influenced, however, by the degree of (im)perfection of the edges of the grains that eventually will merge. One cannot exclude that amorphous GBs may be recrystallized under electron beam irradiation conditions inside the TEM; therefore caution is recommended in the interpretation of the HRTEM data on the GBs formed in CVD graphene. The amorphous GBs may have different electronic structures and different doping structures as compared with the crystalline graphene platelets, as shown by local probe measurements, without any transfer, on the Cu substrate used for CVD.

As shown by UHV STM and electric data, too, the GBs are particularly sensitive to H_2O, and ambient humidity so that, beyond their detrimental effects on the electric transport and mechanical properties, they also constitute an inconvenience from the point of view of environmental stability. They may constitute the route through which, despite the remarkable gas sealing properties of cleaved graphene, various chemical moieties can penetrate underneath the CVD grown graphene and react with the substrate [107].

The recently developed atmospheric pressure CVD methods using molten Cu as the catalyst surface for the decomposition of the hydrocarbons offer several important advantages as compared with CVD on solid Cu:

- smooth and perfect surface, without rolling grooves and GBs in Cu;
- the possibility to use higher growth temperatures;
- regular, self-organized, tile-like arrangement of the growing graphene platelets;
- smooth zigzag-type edges, with higher probability of seamless stitching;
- angular deviations of the order of 2° over distances of the order of $80\,\mu$m in the grown continuous graphene layer.

From the point of view of grain boundary engineering, the CVD using molten Cu seems to offer the most promising procedure for growing large areas of good-quality graphene. However, in this direction, far fewer data are available as compared with the CVD on solid surfaces. Nevertheless, the promise that high-quality, large-area graphene will become widely accessible in a few years does not seem unrealistic at present.

Acknowledgments

The present work was supported in Hungary by the OTKA under grant number K101599. LPB gratefully acknowledges the agreement between the F.R.S.-FNRS (Belgium) and HAS (Hungary) that made possible the cooperation with PhL. Support from the EU FP7 FAEMCAR project is acknowledged.

References

[1] Novoselov K S, Geim A K, Morozov S V, Jiang D, Zhang Y, Dubonos S V, Grigorieva I V and Firsov A A 2004 *Science* **306** 666–9
[2] Geim A K 2009 *Science* **324** 1530–4
[3] Novoselov K 2011 *Rev. Mod. Phys.* **83** 837–49
[4] Bonaccorso F, Sun Z, Hasan T and Ferrari A C 2010 *Nature Photon.* **4** 611–22
[5] Mattevi C, Kim H and Chhowalla M 2011 *J. Mater. Chem.* **21** 3324
[6] Wintterlin J and Bocquet M L 2009 *Surf. Sci.* **603** 1841–52
[7] Bae S *et al* 2010 *Nature Nanotechnol.* **5** 574–8
[8] Biró L P, Nemes-Incze P and Lambin Ph 2012 *Nanoscale* **4** 1824–39
[9] Márk G, Vancsó P, Hwang C, Lambin Ph and Biró L P 2012 *Phys. Rev.* B **85** 125443
[10] Wolf D 1992 *Atomic-Level Geometry of Crystalline Interfaces, Matter Interfaces, Atomic-Level Structure and Properties* ed D Wolf and S Yip (London: Chapman and Hall) 17
[11] Keblinski P, Phillpot S R, Wolf D and Gleiter H 1997 *Nanostruct. Mater.* **9** 651–60
[12] Wolf D 2001 *Curr. Opin. Solid State Mater. Sci.* **5** 435–43
[13] Derlet P and Van Swygenhoven H 2003 *Phys. Rev.* B **67** 014202
[14] Moore A W, Ubbelohde A R and Young D A 1964 *Proc. R. Soc. Lond.* A **280** 153–69
[15] Simonis P, Goffaux C, Thiry P A, Biró L P, Lambin Ph and Meunier V 2002 *Surf. Sci.* **511** 319–22
[16] Červenka J and Flipse C 2009 *Phys. Rev.* B **79** 195429
[17] da Silva Araújo J and Nunes R W 2010 *Phys. Rev.* B **81** 073408
[18] McNaught A D and Wilkinson A 1997 *IUPAC Compendium of Chemical Terminology* 2nd edn (*The 'Gold Book'*) (Oxford: Blackwell)
Nic M, Jirat J and Kosata X 2006 XML on-line corrected version (http://goldbook.iupac.org); updates compiled by A Jenkins (doi:10.1351/goldbook)
[19] Hwang C B, Yoo K, Kim S, Seo E, Yu H and Biró L P 2011 *J. Phys. Chem.* C **115** 22369–74
[20] Carlsson J, Ghiringhelli L and Fasolino A 2011 *Phys. Rev.* B **84** 1–10
[21] Kotakoski J and Meyer J C 2012 *Phys. Rev.* B **85** 195447
[22] Nemes-Incze P, Osváth Z, Kim S J, Hwang C, Lambin Ph, Chapelier C and Biró L P *Carbon* submitted
[23] Brito W, Kagimura R and Miwa R 2012 *Phys. Rev.* B **85** 035404
[24] Ovid'ko I A 2012 *Rev. Adv. Mater. Sci.* **30** 201–24
[25] Banhart F, Kotakoski J and Krasheninnikov A V 2011 *ACS Nano* **5** 26–41
[26] Kim P 2010 *Nature Mater.* **9** 792–3

[27] Feng X, Maier S and Salmeron M 2012 *J. Am. Chem. Soc.* **134** 5662–8
[28] Randle V 2004 *Acta Mater.* **52** 4067–8
[29] Mesaros A, Papanikolaou S, Flipse C F J, Sadri D and Zaanen J 2010 *Phys. Rev.* B **82** 205119
Sadri D 2011 *Nanosci. Nanotechnol. Lett.* **3** 895–901
[30] Malola S, Hakkinen H and Koskinen P 2010 *Phys. Rev.* B **81** 165447
[31] Liu Y and Yakobson B I 2010 *Nano Lett.* **10** 2178–83
[32] Lahiri J, Lin Y, Bozkurt P, Oleynik I I and Batzill M 2010 *Nature Nanotechnol.* **5** 326–9
[33] Yazyev O V and Louie S G 2010 *Phys. Rev.* B **81** 195420
[34] Liu T H, Gajewski G, Pao C W, Liu T H and Chang C C 2011 *Carbon* **49** 2306–17
[35] Read W T and Shockley W 1950 *Phys. Rev.* **78** 275–89
[36] Roscoe C and Thomas J M 1966 *Carbon* **4** 383–4
[37] Li X F, Wang L L, Chen K Q and Luo Y 2010 *J. Phys. Chem.* C **115** 12616–24
[38] Mele E J 2010 *Phys. Rev.* B **81** 161405
[39] da Silva Araujo J and Nunes R W 2010 *Phys. Rev.* B **81** 073408
[40] http://nanoprobes.aist-nt.com/apps/HOPG%20info.htm (accessed: 8 June 2012)
[41] www.2spi.com/catalog/new/hopgsub.php (accessed: 8 June 2012)
[42] www.momentive.com/Products/Main.aspx?id=22817 (accessed: 8 June 2012)
[43] Albrecht T, Mizes H and Nogami J 1988 *Appl. Phys. Lett.* **52** 362–4
[44] Clemmer C R and Beebe T P 1991 *Science* **251** 640
[45] Červenka J, Katsnelson M I and Flipse C F J 2009 *Nature Phys.* **5** 840–4
[46] Wang Y, Ye Y and Wu K 2006 *Surf. Sci.* **600** 729–34
[47] Biedermann L, Bolen M, Capano M, Zemlyanov D and Reifenberger R 2009 *Phys. Rev.* B **79** 125411
[48] Bernhardt T M, Kaiser B and Rademann K 1998 *Surf. Sci.* **408** 86–94
[49] Biró L P, Nemes-Incze P, Dobrik G, Hwang C and Tapasztó L 2011 *Diamond Rel. Mater.* **20** 1212–17
[50] Varchon F, Mallet P, Magaud L and Veuillen J Y 2008 *Phys. Rev.* B **77** 165415
[51] Starke U and Riedl C 2009 *J. Phys.: Condens. Matter.* **21** 134016
[52] N'Diaye A T, Engler M, Busse C, Wall D, Buckanie N, Meyer zu Heringdorf F J, van Gastel R, Poelsema B and Michely T 2009 *New J. Phys.* **11** 023006
[53] Coraux J, N'Diaye A T, Busse C and Michely T 2008 *Nano Lett.* **8** 565–70
[54] Robertson J 1986 *Adv. Phys.* **35** 317–74
[55] Robertson J and O'Reilly E P 1987 *Phys. Rev.* B **35** 2946–57
[56] Ferrari A C and Robertson J 2000 *Phys. Rev.* B **61** 95–107
[57] Robertson J 2002 *Mater. Sci. Eng.* R **37** 129–281
[58] Gómez-Navarro C, Meyer J C, Sundaram R S, Chuvilin A, Kurasch S, Burghard M, Kern K and Kaiser U 2010 *Nano Lett.* **10** 1144–8
[59] Kotakoski J, Krasheninnikov A V, Kaiser U and Meyer J C 2011 *Phys. Rev. Lett.* **106** 105505
[60] Kotakoski J, Meyer J, Kurasch S, Santos-Cottin D, Kaiser U and Krasheninnikov A V 2011 *Phys. Rev.* B **83** 245420
[61] Kurasch S, Kotakoski J, Lehtinen O J, Skakalova V, Smet J H, Krill C, Krasheninnikov A V and Kaiser U 2012 *Nano Lett.* **12** 3168–73
[62] Li X, Magnuson C W, Venugopal A, Tromp R M, Hannon J B, Vogel E M, Colombo L and Ruoff R S 2011 *J. Am. Chem. Soc.* **133** 2816–9
[63] Li X 2009 *Science* **324** 1312–4
[64] Wofford J M, Nie S, McCarty K F, Bartelt N C and Dubon O D 2010 *Nano Lett.* **10** 4890–6
[65] Bhaviripudi S, Jia X, Dresselhaus M S and Kong J 2010 *Nano Lett.* **10** 4128–33
[66] Li X 2009 *Science* **324** 1312–4
[67] Wu B, Geng D, Guo Y, Huang L, Xue Y, Zheng J, Chen J, Yu G, Liu Y, Jiang L and Hu W 2011 *Adv. Mater.* **23** 3522–25
[68] Li X *et al* 2010 *Nano Lett.* **10** 4328–34

[69] Kertész K *et al* 2012 *Appl. Phys. Lett.* **100** 213103
[70] Liu W, Li H, Xu C, Khatami Y and Banerjee K 2011 *Carbon* **49** 4122–30
[71] Vlassiouk I, Regmi M, Fulvio P, Dai S, Datskos P, Eres G and Smirnov S 2011 *ACS Nano* **5** 6069–76
[72] Gao L, Ren W, Zhao J, Peng Ma L, Chen Z, Gao L, Ren W and Peng Ma L 2012 *Appl. Phys. Lett.* **97** 183109
[73] Geng D, Wu B, Guo Y, Huang L, Xue Y, Chen J, Yu G, Jiang L, Hu W and Liu Y 2012 *Proc. Natl Acad. Sci.USA* **109** 7992–6
[74] Wu Y A, Fan Y, Speller S, Creeth G L, Sadowski J T, He K, Robertson A W, Allen C S and Warner J H 2012 *ACS Nano* **6** 5010–7
[75] Nie S, Wofford J, Bartelt N, Dubon O and McCarty K 2011 *Phys. Rev.* B **84** 155425
[76] Zhao L, Rim K T, Zhou H, He R, Heinz T F, Pinczuk A, Flynn G W and Pasupathy A N 2011 *Solid State Commun.* **151** 509–13
[77] Ogawa Y, Hu B, Orofeo C M, Tsuji M, Ikeda K, Mizuno S, Hibino H and Ago H 2012 *J. Phys. Chem. Lett.* **3** 219–6
[78] Rasool H I, Song E B, Mecklenburg M, Regan B C, Wang K L, Weiller B H and Gimzewski J K 2011 *J. Am. Chem. Soc.* **133** 12536–43
[79] He R, Zhao L, Petrone N, Kim K S, Roth M, Hone J, Kim P, Pasupathy A and Pinczuk A 2012 *Nano Lett.* **12** 2408–13
[80] Huang P Y *et al* 2011 *Nature* **469** 389–92
[81] Kim K, Lee Z, Regan W, Kisielowski C, Crommie M F and Zettl A 2011 *ACS Nano* **5** 2142–6
[82] Tapasztó L, Nemes-Incze P, Dobrik G, Jae Yoo K, Hwang C and Biró L P 2012 *Appl. Phys. Lett.* **100** 053114
[83] Gao L, Guest J R and Guisinger N P 2010 *Nano Lett.* **10** 3512–6
[84] Zhang Y, Gao T, Gao Y, Xie S, Ji Q, Yan K, Peng H and Liu Z 2011 *ACS Nano* **5** 4014–22
[85] Nemes-Incze P, Yoo K J, Tapasztó L, Dobrik G, Lábár J, Horváth Z E, Hwang C and Biró L P 2011 *Appl. Phys. Lett.* **99** 023104
[86] Yakobson B I and Ding F 2011 *ACS Nano* **5** 1569–74
[87] Yu Q *et al* 2011 *Nature Mater.* **10** 443–9
[88] Jauregui L A, Cao H, Wu W, Yu Q and Chen Y P 2011 *Solid State Commun.* **151** 1100–4
[89] Kumar S B and Guo J 2012 *Nano Lett.* **12** 1362–6
[90] Yazyev O V and Louie S G 2010 *Nature Mater.* **9** 806–9
[91] Gunlycke D and White C T 2011 *Phys. Rev. Lett.* **106** 136806
[92] Bryan S E, Yang Y and Murali R 2011 *J. Phys. Chem.* C **115** 10230–5
[93] Tsen A W, Brown L, Levendorf M P, Ghahari F, Huang P Y, Havener R W, Ruiz-Vargas C S, Muller D, Kim P and Park J 2012 *Science* **336** 1143–6
[94] Kolesnikov D V and Osipov V A 2012 *Europhys. Lett.* **100** 26004
[95] Bagri A, Kim S, Ruoff R S and Shenoy V B 2011 *Nano Lett.* **11** 3917–21
[96] Balandin A A, Ghosh S, Bao W, Calizo I, Teweldebrhan D, Miao F and Lau C N 2008 *Nano Lett.* **8** 902–7
[97] Ghosh S, Calizo I, Teweldebrhan D, Pokatilov E P, Nika D L, Balandin A, Bao W, Miao F and Lau C N 2008 *Appl. Phys. Lett.* **92** 151911
[98] Cai W, Moore A L, Zhu Y, Li X, Chen S, Shi L and Ruoff R S 2010 *Nano Lett.* **10** 1645–51
[99] Seol J H *et al* 2010 *Science* **328** 213–6
[100] Vlassiouk I, Smirnov S, Ivanov I, Fulvio P F, Dai S, Meyer H, Chi M, Hensley D, Datskos P and Lavrik N V 2011 *Nanotechnology* **22** 275716
[101] Cançado L G, Takai K, Enoki T, Endo M, Kim Y, Mizusaki H, Jorio A, Coelho L N, Magalhães-Paniago R and Pimenta M 2006 *Appl. Phys. Lett.* **88** 163106
[102] Balandin A A 2011 *Nature Mater.* **10** 569–81
[103] Brito W H, Kagimura R and Miwa R H 2011 *Appl. Phys. Lett.* **98** 213107
[104] Brito W H, Kagimura R and Miwa R H 2012 *Phys. Rev.* B **85** 035404

[105] Chan J, Venugopal A, Pirkle A, McDonnell S, Hinojos D, Magnuson C W, Ruoff R S, Colombo L, Wallace R M and Vogel E 2012 *ACS Nano* **4** 3224–9
[106] Yang Y and Murali R 2011 *Appl. Phys. Lett.* **98** 093116
[107] Duong D L *et al* 2012 *Nature* **490** 235–9
[108] Gran Table R, Shenoy V B and Ruoff R S 2010 *Science* **330** 946–8
[109] Zhang J, Zhao J and Lu J 2012 *ACS Nano* **6** 2704–11
[110] Kim K, Artyukhov V I, Regan W, Liu Y, Crommie M F, Yakobson B I and Zettl A 2012 *Nano Lett.* **12** 293–7